LOW VOLTAGE RIDE THROUGH CONTROL FOR THE BRUSHLESS DOUBLY – FED INDUCTION GENERATORS

MASTER OF SCIENCE THESIS
NOVEMBER 2017

BY

SHAOCHUAN ZHANG

LOW VOLTAGE RIDE THROUGH CONTROL FOR THE BRUSHLESS DOUBLY – FED INDUCTION GENERATORS

MASTER OF SCIENCE THESIS
NOVEMBER 2017

BY

SHAOCHUAN ZHANG

Supervisors:

Dr.ir. Henk Polinder
Dr.ir. Jianning Dong
Udai Shipurkar
Mahyar Gholizade

Thesis Committee Members:

Dr.ir. Henk Polinder
Dr.ir. Jianning Dong
Dr.ir. Milos Cvetkovic

DC systems, Energy conversion & Storage
Department of Electrical Sustainable Energy
Faculty of Electrical Engineering, Mathematics and Computer Science
Delft University of Technology

November 24, 2017

ABSTRACT

STABILITY and security of the grid are two vital aspects of energy supply. To keep the grid stable, it is necessary that the electricity plant can control and protect the mechanism. In the past, traditional plants could meet these requirements. Nowadays, the share of sustainable power sources in total electricity generation has become so important that these sources must keep the grid stable. A significant part of these requirements is the Low Voltage Ride Through (LVRT) capability of the sustainable energy plant. When some large loads are connected to the grid or as a result of grid faults like lightning strikes or short circuits, short–term voltage dip may occur. This low voltage dip condition plans to be simulated and the behaviours of Brushless Doubly-Fed Induction Generator (B-DFIG) should be improved in this situation. This thesis is going to realize this goal that after the improvement, when low voltage dip occurs, it is not necessary to disconnect the generator from the grid.

The thesis is organized as follows: Firstly, the B-DFIG modelling is implemented, including the steady state modelling by equivalent circuits and the dynamic modelling by differential equations. The steady and transient state characteristic of B-DFIG can be studied by equivalent circuits and dynamic models respectively. Secondly, the control algorithm is added to the power electronic converter to control the machine in a stable and responsive manner. Thirdly, simulations of both full voltage and low voltage dip conditions are done to compare B-DFIG behaviours between these two different simulation conditions. Unexpected performance like large transient current will occur under low voltage dip condition. Fourthly, the LVRT control algorithm is added to the controller of B-DFIG for improving the behaviours of B-DFIG in low voltage dip condition based on some constraints and assumptions. Finally, experiments are executed to verify this result.

Index Terms — Brushless Doubly-Fed Induction Generator, Low Voltage Ride Through, security, stability

Acknowledgements

Firstly, I would like to thank my supervisor Henk Polinder for his help and guidance for the thesis and presentation. Both meeting and discussion with him always give me a lot of enlightenment.

Secondly, I also want to thank my daily superviosr Jianning Dong for his help in my project and thesis. Every time when I face a problem, he will guide me in a correct direction patiently. He will also give me many possibilities to choose and try based on my thought, which exercises my innovation a lot. It is the best way for education.

Thirdly, I would like to thank my phd superviosr Udai Shipurkar for the guidance in project and especial in experiment. He is a supportive person. He teaches me the operation in experiment step by step and we are troubleshooting together. Following with him, I am very happy in doing my project. In addition, I also thank my another phd supervisor Mahyar Gholizade. Although he was my supervisor only for 5 months, he told me a lot of knowledge and made me from nothing to clarity. He gave me a lot of self-confidence which makes me go further.

Fourthly, I would like to thank the technicians Joris Koeners, Harrie Olsthoorn and Bart Roodenburg. They give me a lot of support on the operation of experiment, safety awareness and components ordering. Without them, I cannot finish the experiment successfully.

Fifthly, I am willing to thank all of my master classmates and my other friends in the Netherlands. It my honor to know them and I will remember these two years time together with them forever.

Finally, I want to thank my parents who give me the life and financial support. Although they cannot guide me in an academic level, they give me their best. They are willing to answer any of the confusion in my life and do extremely support me.

List of Symbols

p_p	Pole pairs in power winding
p_c	Pole pairs in control winding
n_{pw}	Transformation ratio between power winding and rotor
n_{cw}	Transformation ratio between rotor and control winding
L'_p	Converted inductance in power winding
b_p	Field generated by power winding
b_c	Field generated by control winding
ω_p	Electric angular frequency in power winding
ω_c	Electric angular frequency in control winding
α_p	Phase angle of power winding
α_c	Phase angle of control winding
ω_m	Mechanical angular frequency of rotor
ω_r	Electric angular frequency in rotor
s_p	Slip in power winding
s_c	Slip in control winding
f_p	Electric frequency in power winding
f_c	Electric frequency in control winding
f_r	Electric frequency in rotor

f_m	Mechanical frequency of rotor
n	Speed in rpm of rotor
s	Slip of the machine
R_p	Resistance in power winding
R_c	Resistance in control winding
$R_{r,n}$	Resistance in the n^{th} rotor loop
L_p	Inductance in power winding
$L_{p,m}$	Main inductance in power winding
$L_{p,\sigma}$	Leakage inductance in power winding
L_c	Inductance in control winding
$L_{c,m}$	Main inductance in control winding
$L_{c,\sigma}$	Leakage inductance in control winding
$L_{r,n}$	Inductance in the n^{th} rotor loop
$L_{r,np}$	Main inductance in the n^{th} rotor loop (between rotor and power winding)
$L_{r,nc}$	Main inductance in the n^{th} rotor loop (between rotor and control winding)
$L_{r,n\sigma}$	Leakage inductance in the n^{th} rotor loop
$M_{p,rn}$	Mutual inductance between power winding and the n^{th} rotor loop
$M_{c,rn}$	Mutual inductance between control winding and the n^{th} rotor loop
N_l	Total number of loops
N_n	Total number of nests
L_σ	Converted leakage inductance in control winding
θ_m	Mechanical position angle of rotor
T_{pe}	Electric torque produced by power winding
T_{ce}	Electric torque produced by control winding
T_e	Electric torque produced by the machine

T_l	Load torque
u_p	Phase voltage in power winding
u_c	Phase voltage in control winding
i_{pd}	d-axis current in power winding
i_{pq}	q-axis current in power winding
i_{cd}	d-axis current in control winding
i_{cq}	q-axis current in control winding
θ^c_{flux}	Flux position angle in control winding
λ_{pd}	d-axis flux in power winding
λ_{pq}	q-axis flux in power winding
λ_{cd}	d-axis flux in control winding
λ_{cq}	q-axis flux in control winding
U_{dc}	DC-link voltage
N_{ph}	Number of phases
N_{ss}	Number of stator slots
N_{rs}	Number of rotor slots
q_r	Rotor loops per nest
N_p	Turns per phase in power winding
N_c	Turns per phase in control winding

LIST OF ACRONYMS

LVRT	Low Voltage Ride Through
B-DFIG	Brushless Doubly-Fed Induction Generator
DFIG	Doubly-Fed Induction Generator
B-DFIM	Brushless Doubly-Fed Induction Machine
PW	Power Winding
CW	Control Winding
IRTF	Ideal Rotating Transformer
VOC	Voltage Oriented Control
FOC	Field Oriented Control
GPIO	General Propose Input Output
PSU	Power Supply Unit
FAST	Flux Angle Speed Torque

LIST OF FIGURES

LIST OF TABLES

CONTENTS

1

INTRODUCTION

1.1. BACKGROUND

NOWADAYS, it is significant to keep the grid stable and secure. However, some special conditions always occur in the grid. Low voltage dip is the most common phenomenon. As a generator, Brushless Doubly-Fed Induction Generator (B-DFIG) should have the ability of standing the low voltage dip condition and when faults occur, it needs to be connected from the grid. This ability is called Low Voltage Ride Through (LVRT). Therefore, simulating the machine in low voltage dip condition is very important to check whether B-DFIG has this ability.

Wind turbines can be divided into *Fixed speed wind turbines* and *Variable speed wind turbines* [1] according to the generator used for power extraction. In a large wind turbine, compared with the constant speed wind turbine, people always prefer to use the variable speed wind turbine which has not only better grid code connection compliance but also more efficiency in power collection. A kind of variable speed wind turbine is the Doubly-Fed Induction Generator (DFIG) which contains a wound rotor induction generator connected to a power electronic converter via brushes and slip rings. The rotor winding can both deliver and absorb energy according to the speed of rotor.

It is known that DFIG is commonly used in some sustainable energy generation such as wind turbines, because it can operate normally in variable speed of wind and generate fixed–frequency electricity (50 Hz). However, DFIG has less reliability and needs more maintenance due to the use of brushes and slip rings. In contrast, B-DFIG keeps all of the benefits of DFIG such as the ability to exchange active and reactive power with grid but without brushes and slip rings and thus achieve higher reliability and lower operational cost. In addition, B-DFIG does not have a wound rotor, but a special rotor construction which is used for coupling magnetically to two stator windings. These two stator windings are placed in the same stator. In B-DFIG, this kind of rotor design does not need to be connected to an external power supply, thus slip rings and brushes are not necessary.

The development of B-DFIG began at the start of 20th century. At that time, power electronic technology was not very popular for the control of electrical machines. People could use two cascade connected slip ring induction machines to control the speed. In 1907, Hunt proposed a kind of machine which contained two stator windings and a special rotor structure in [2]. This machine did not have any brush and slip ring and its speed could be controlled by resistors which were connected to one of the stator winding. The machine is called Brushless Doubly-Fed Induction Machine (B-DFIM) and it can be as a motor or a generator. Especially, in wind turbine application, people usually use this machine as a generator to deliver electricity. Thus it is called as Brushless Doubly-Fed Induction Generator (B-DFIG) in this thesis.

In 1970s, further achievements had been made on B-DFIM when Broadway *et al.* raised caged rotor (nest loop) in [3], which is still used in B-DFIM nowadays. In addition, they also studied the equivalent circuit of B-DFIM and analyzed its behaviours in steady state. They paid more attention on the operation of the machine in the synchronous mode. In [4], Kusko and Somuah researched the operation of the single-frame brushless induction motor with a rectifier-inverter to control its speed by slip-power pump back to the line. Until this time, all of the stator designs used a single stator that yielded both field of different pole numbers. However, in 1990, Rochelle *et al.* compared the substitutes of the stator winding design and found electrically isolated windings had more advantages [5]. Therefore, after that, all of B-DFIM started to use this kind of design.

Wallace *et al* at Oregan State University created a dynamic model for B-DFIM in [6] and used simulation models to analyze the behaviours of B-DFIM in the middle of 1980s in [7]. Li *et al.* studied a two-axis model which is suitable for dynamic research [8] and displayed the outcome of dynamic simulations [9]. Moreover, Williamson *et al.* showed a generalized mathematical model for the B-DFIM which is working in the synchronous mode [10][11] at Cambridge University. In 1994, Zhou and Spee found the d-q axis model could rotate at synchronous speed following with the d-q axis current [12]. However, this reference frame did not have any physical meaning. The values of transformed d-q axis components were fixed. Through this study, people created the first field orientated controller for the B-DFIG. From that time, B-DFIG could be controlled by multiple strategies. In 2002, Poza *et al.* created a vector control algorithm [13] according to the Power Winding Flux.

Until this time, people did not pay much attention on LVRT performance of the B-DFIG. Under symmetrical voltage dips [14], the dynamic behaviours of B-DFIG had been studied by Shao *et al.* However, this study had its own limit that it did not consider the subsequent voltage increase in the grid and there was not any method to improve the machine's behaviours. In 2011, people displayed a control method which let the machine have the capability to ride through low voltage faults [15]. Furthermore, this control method had been extended for asymmetrical low voltage dips [16].

This thesis focuses on the study of the effect of the grid fault (LVRT) on B-DFIG. The study contains improvement of B-DFIG behaviours and the protection of the power electronic converter during the low voltage dip.

1.2. OBJECTIVES

THE main objective of this thesis is to improve the behaviour of B-DFIG under low voltage dip condition. In other words, the LVRT ability of B-DFIG should be improved by the proposed method in this thesis.

Low voltage dip condition occurs when the grid is connected to large loads or undergoes lightning strikes or short circuits. Without the LVRT control algorithm, the large transient current caused by low voltage dip will be harmful to the power electronic converter. Therefore, it is rather necessary to propose an effective LVRT control algorithm to solve the problem. After improvement, the current can be controlled below the maximum value under low voltage dip condition, so that the power electronic converter will not be destroyed and the machine will not need to be disconnected from the grid.

1.3. METHODOLOGY

IN order to realize the objective of improving the behaviour of B-DFIG under low voltage dip condition, a series of steps are proposed as follows.

B-DFIG steady state model

To understand the operating principle of B-DFIG, three different modes of B-DFIG are illustrated: simple, cascade and synchronous modes. This thesis mainly focuses on the synchronous mode since it is the most popular mode in industry.

Firstly, to illustrate the operating principle of B-DFIG in synchronous mode, mathematical equations are derived to express the relationship between different variables. Secondly, to investigate the steady state characteristics of the machine, different kinds of equivalent circuits are built by forming phasor equations of the machine. The parameters are derived from the geometry of B-DFIG. The equations and equivalent circuits are based on [17].

The result of B-DFIG steady state model will be indicated in Chapter 2 in this thesis.

B-DFIG dynamic model

In order to investigate the transient state characteristic of B-DFIG, the dynamic model is built.

Firstly, differential equations are presented based on [18] to show the relationship between variables in transient state; Then the block diagram is built by connecting blocks based on these equations.

The result of B-DFIG dynamic model will be displayed in Chapter 3 in this thesis.

B-DFIG control strategy

In normal condition, the control strategy is quite necessary to the power electronic converter in order to ensure B-DFIG to operate at the synchronous mode. The control strategy is shown based on [18] and added to the model and the feasibility of the proposed control strategy is checked based on given conditions in the model.

The accomplishment of B-DFIG control strategy will be shown in Chapter 4 in this thesis.

B-DFIG LVRT simulation

Two different situations, full voltage and low voltage dip, are included in the simulation to compare the performance of B-DFIG in full voltage and low voltage dip condition based on constraints and assumptions. Compared with B-DFIG behaviour in normal condition, there is a large transient current in stator winding in low voltage dip condition, which is harmful to the power electronic converter. In addition, some analyses are displayed to explain the reason.

The development of B-DFIG LVRT simulation will be written in Chapter 5 in this thesis.

B-DFIG LVRT control algorithm

Due to the large transient current in low voltage dip condition, method will be proposed to solve this problem. Therefore, firstly, the factors which influence B-DFIG behaviour should be known clearly. Secondly, based on studies of influencing factors, constraints and assumptions, the LVRT control algorithm will be introduced step by step and added in B-DFIG controller. Finally, results and analyses will be given to testify the rationality of LVRT control algorithm.

The development of B-DFIG LVRT control algorithm will be presented in Chapter 6 in this thesis.

B-DFIG LVRT experiment

Firstly, some parameters such as resistance and inductance in different windings are measured through different tests. Secondly, low voltage dip is built at the terminal of B-DFIG in the experiment. A voltage divider circuit is used, which contains two inductors and two contactors. Contactors always work in high voltage environment, hence another control circuit is used to control the contactor. Thirdly, based on the power electronic converter and control strategy proposed in Tim Dave Strous' PhD thesis [18], the same test conditions as Chapter 5 are given in experiment, which are full voltage condition and low voltage dip condition. Finally, after measuring B-DFIG behaviours in the experiment, analyses are given to explain the performance and show the consistency between simulation and experiment.

The development of B-DFIG LVRT experiment will be described in Chapter 7 in this thesis.

1.4. CONTRIBUTION

BASICALLY, this thesis is divided into two parts: the first one is building the model of B-DFIG including B-DFIG steady state model, dynamic model and control strategy (Chapter 2-4), which is mainly based on the method introduced in Udai Shipurkar's master thesis [17] and Tim Dave Strous' PhD thesis [18]; the second one is LVRT control including LVRT simulation, control algorithm and experiment (Chapter 5-7). LVRT control should be mainly focused on due to the objectives and contributions in this thesis are listed below.

In simulation, based on B-DFIG model in [18], B-DFIG behaviours in both full voltage and low voltage dip conditions are simulated and proper LVRT control algorithm is proposed to improve B-DFIG behaviour. In addition, the microcontroller is programmed to control the power relays and contactors producing low voltage dip at the terminal of B-DFIG in experiment. Then B-DFIG behaviours are measured under both full voltage and low voltage dip conditions and the results can prove the rationality of LVRT control algorithm in simulation.

REFERENCES

[1] O. Anaya-Lara, N. Jenkins, J. B. Ekanayake, P. Cartwright, and M. Hughes, *Wind energy generation: modelling and control* (John Wiley & Sons, 2011).

[2] L. J. Hunt, *A new type of induction motor,* Journal of the Institution of Electrical Engineers **39**, 648 (1907).

[3] A. Broadway and L. Burbridge, *Self-cascaded machine: a low-speed motor or high-frequency brushless alternator,* in *Proceedings of the Institution of Electrical Engineers*, Vol. 117 (IET, 1970) pp. 1277–1290.

[4] A. Kusko and C. B. Somuah, *Speed control of a single-frame cascade induction motor with slip-power pump back,* IEEE Transactions on Industry Applications , 97 (1978).

[5] P. Rochelle, R. Spee, and A. K. Wallace, *The effect of stator winding configuration on the performance of brushless doubly-fed machines in adjustable speed drives,* in *Industry Applications Society Annual Meeting, 1990., Conference Record of the 1990 IEEE* (IEEE, 1990) pp. 331–337.

[6] A. K. Wallace, R. Spee, and H. K. Lauw, *Dynamic modeling of brushless doubly-fed machines,* in *Industry Applications Society Annual Meeting, 1989., Conference Record of the 1989 IEEE* (IEEE, 1989) pp. 329–334.

[7] R. Spee, A. K. Wallace, and H. K. Lauw, *Performance simulation of brushless doubly-fed adjustable speed drives,* in *Industry Applications Society Annual Meeting, 1989., Conference Record of the 1989 IEEE* (IEEE, 1989) pp. 738–743.

[8] R. Li, A. Wallace, R. Spee, and Y. Wang, *Two-axis model development of cage-rotor brushless doubly-fed machines,* IEEE Transactions on Energy Conversion **6**, 453 (1991).

[9] R. Li, A. Wallace, and R. Spee, *Dynamic simulation of brushless doubly-fed machines,* IEEE Transactions on Energy Conversion **6**, 445 (1991).

[10] S. Williamson, A. Ferreira, and A. Wallace, *Generalised theory of the brushless doubly-fed machine. part 1: Analysis,* IEE Proceedings-Electric Power Applications **144**, 111 (1997).

[11] S. Williamson and A. Ferreira, *Generalised theory of the brushless doubly-fed machine. part 2: Model verification and performance,* IEE Proceedings-Electric Power Applications **144**, 123 (1997).

[12] D. Zhou and R. Spee, *Synchronous frame model and decoupled control development for doubly-fed machines,* in *Power Electronics Specialists Conference, PESC'94 Record., 25th Annual IEEE,* Vol. 2 (IEEE, 1994) pp. 1229–1236.

[13] J. Poza, E. Oyarbide, and D. Roye, *New vector control algorithm for brushless doubly-fed machines,* in *IECON 02 [Industrial Electronics Society, IEEE 2002 28th Annual Conference of the]*, Vol. 2 (IEEE, 2002) pp. 1138–1143.

[14] S. Shao, E. Abdi, and R. McMahon, *Dynamic analysis of the brushless doubly-fed induction generator during symmetrical three-phase voltage dips,* in *Power Electronics and Drive Systems, 2009. PEDS 2009. International Conference on* (IEEE, 2009) pp. 464–469.

[15] S. Shao, T. Long, E. Abdi, R. McMahon, and Y. Wu, *Symmetrical low voltage ride-through of the brushless doubly-fed induction generator,* in *IECON 2011-37th Annual Conference on IEEE Industrial Electronics Society* (IEEE, 2011) pp. 3209–3214.

[16] T. Long, S. Shao, E. Abdi, R. A. McMahon, and S. Liu, *Asymmetrical low-voltage ride through of brushless doubly fed induction generators for the wind power generation,* IEEE Transactions on Energy Conversion **28**, 502 (2013).

[17] U. Shipurkar, *Brushless doubly fed induction generator based wind turbine drive-train under grid fault conditions,* (2014).

[18] T. Strous, *Brushless doubly fed induction machines for wind turbine drive-train applications,* (2016).

2

B-DFIG STEADY STATE MODEL

2.1. INTRODUCTION

To get the steady state characteristics of B-DFIG, the steady state model of B-DFIG is built in this chapter. First, basic operating principles of B-DFIG in simple, cascade and synchronous modes are illustrated. In addition, equations describing relationships between different variables in synchronous mode are derived. Different equivalent circuits of B-DFIG are built to model the steady state operation, using numerical calculations.

2.2. OPERATING PRINCIPLES OF B-DFIG

B-DFIG has two 3-phase stator windings with different pole pair numbers. The structure of B-DFIG is shown in Figure 2.1. One of the stator windings is called 'Power Winding' and the other is called 'Control Winding'. Power winding (PW) is directly connected to the grid with fixed frequency and voltage. Control winding (CW) is connected through a partially rated power electronic converter with various frequencies and voltage. The rotor is cage design which does not need to be connected to the external circuit. Thus, there is no brush and slip ring.

When the PW has p_p pole pairs and CW has p_c pole pairs, B-DFIG can operate as an induction machine with either p_p or p_c pole pairs. This mode is called simple induction mode and can be realized by making either PW or CW be connected to the grid and leaving the other one open circuit. When B-DFIG operates in this mode, its behaviours will be like an induction machine, except the performance will be poor [1]. When one of the stator winding is short circuit and the other stator winding is connected to the power supply, B-DFIG will work as an induction machine with p_p+p_c pole pairs, which is operating in the cascade mode. These two modes of operation (simple and cascade modes) are asynchronous modes and the speed of B-DFIG is dependent on the load torque. If both stator windings are connected to the grid, B-DFIG works in synchronous mode which is the desirable operating mode.

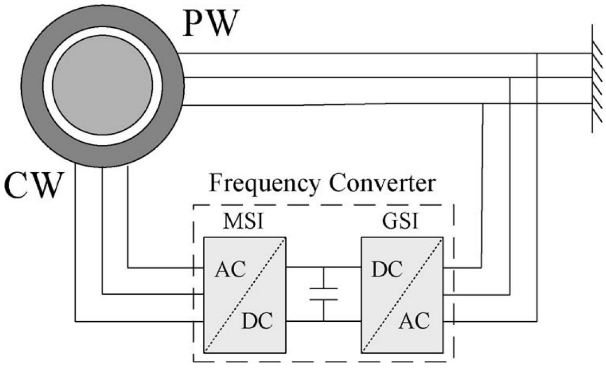

Figure 2.1: Structure of B-DFIG [2]

2.2.1. SIMPLE MODE OF OPERATION

In this mode, B-DFIG behaves like an induction machine. If PW is connected to the grid and CW is open circuit, there are p_p pole pairs and if CW is connected to the grid and PW is open circuit, there are p_c pole pairs. Experiment is implemented on this operating mode and it is based on the equivalent circuit in Figure 2.2. This equivalent circuit is proposed in [3].

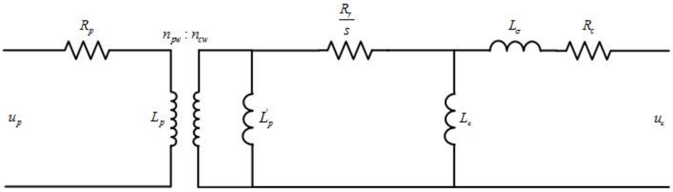

Figure 2.2: Equivalent Circuit of B-DFIG [3]

There are two transformation ratios between PW and rotor and rotor and CW in B-DFIG respectively. In Figure 2.2, both of them are converted into PW side, which are represented by $n_{pw} : n_{cw}$. n_{pw} and n_{cw} mean the transformation ratio between PW and rotor, rotor and CW respectively and L_p' means the converted inductance of PW. All of leakage inductance is transformed into CW. In that case, the equivalent circuit is more suitable for development of the control part. Figure 2.3 shows the phase voltage and current of B-DFIG at 100 V in PW and CW open circuit, 100 V in CW and PW open circuit respectively. These measurements are done in experiment environment.

The parameters of the machine are shown in Table 2.1 and the whole measurement process will be given detailedly in Chapter 7.2. Table 2.2 shows the measurement results from Figure 2.3.

R_p (Ω)	L_p (H)	L'_p (H)	$n_{pw} : n_{cw}$	R_r (Ω)	R_c (Ω)	L_σ (H)	L_c (H)
0.77	0.084	0.0496	1.3	1.968	0.7	0.023	0.1027

Table 2.1: Parameters of B-DFIG

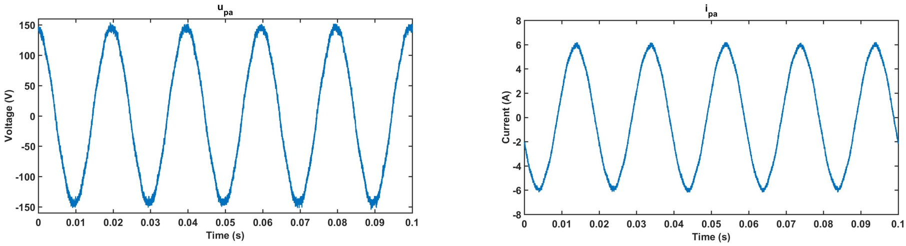

(a) PW Phase Voltage (b) PW Phase Current

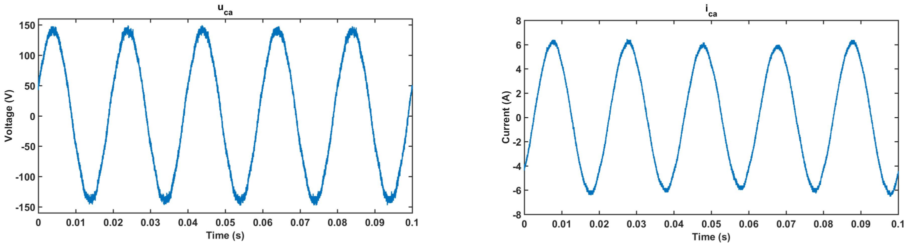

(c) CW Phase Voltage (d) CW Phase Current

Figure 2.3: PW and CW Phase Voltage and Current in Simple Mode

Values	u_a (V)	i_a (A)	f (Hz)	p	n_s (rpm)	n_{rated} (rpm)	s
CW open circuit	100	4.3	50	3	1000	989	0.011
PW open circuit	100	4.3	50	2	1500	1430	0.047

Table 2.2: Measurement Results in Simple Mode

In Figure 2.3, B-DFIG behaves like an induction machine with 3 pole pairs ((a) and (b)) and 2 pole pairs ((c) and (d)) in simple mode. In Figure 2.4, it also can be observed that the equivalent circuits are like induction machines. These equivalent circuits are derived from Figure 2.2.

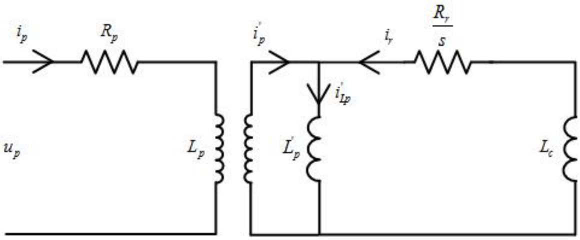

(a) CW Open Circuit

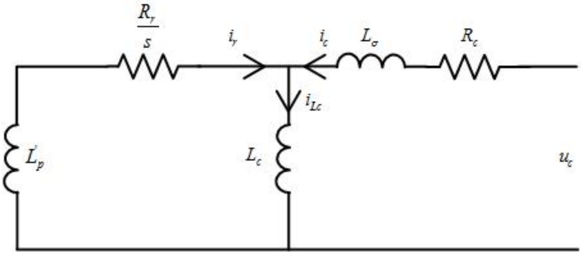

(b) PW Open Circuit

Figure 2.4: B-DFIG Equivalent Circuit in Simple Mode

2.2.2. Cascade Mode of Operation

In this mode, B-DFIG also behaves like an induction machine. Whatever PW or CW is connected to the grid, there are p_p+p_c pole pairs. Figure 2.5 shows phase voltage and current of the machine at 100 V in PW and CW short circuit. The machine parameters and test environment are the same as that in Chapter 2.2.1. Table 2.3 indicates the measurement results from Figure 2.5.

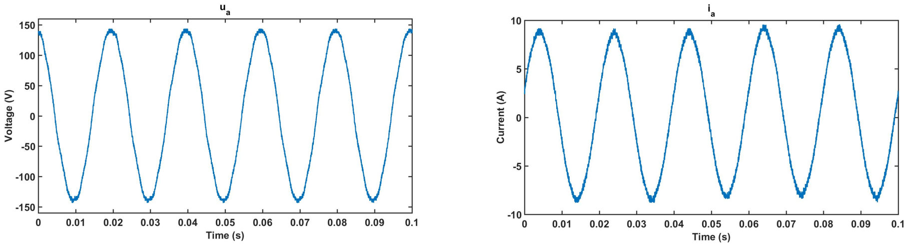

(a) Phase Voltage (b) Phase Current

Figure 2.5: Phase Voltage and Current in Cascade Mode

Values	u_a (V)	i_a (A)	f (Hz)	p	n_s (rpm)	n_{rated} (rpm)	s
CW short circuit	100V	6.36A	50Hz	5	600	594	0.01

Table 2.3: Measurement Results in Cascade Mode

In Figure 2.5, B-DFIG behaves like an induction machine with 5 pole pairs in cascade mode. In Figure 2.6, the equivalent circuit is observed like an induction machine. This equivalent circuit is also derived from Figure 2.2.

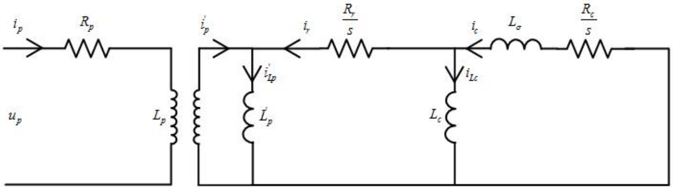

Figure 2.6: B-DFIG Equivalent Circuit in Cascade Mode (CW short circuit)

2.2.3. SYNCHRONOUS MODE OF OPERATION

The synchronous operating mode of B-DFIG comes from the coupling of two stator windings with different pole pairs through the rotor [4]. In this situation, PW is connected to the grid directly and CW is connected to a partially power electronic converter, which is shown as Figure 2.1.

In this occasion, the fundamental fields in the air gap generated by PW and CW are shown in (2.1) and (2.2):

$$b_p(\theta,t) = \hat{B}_p cos(\omega_p t - p_p\theta + \alpha_p) \tag{2.1}$$

$$b_c(\theta,t) = \hat{B}_c cos(\omega_c t + p_c\theta + \alpha_c) \tag{2.2}$$

in which b_p and b_c indicate the fields generated by PW and CW with p_p and p_c pole pairs. ω_p and ω_c are the excitation frequencies and α_p and α_c are phase angles. In this thesis, the convention is that when the rotating direction of CW field is different from that of PW field, the frequency of CW is positive. That is the reason why the sign of $p_c\theta$ in (2.2) is opposite to that of $p_p\theta$ in (2.1). If the rotor rotates with an angular speed ω_m, the equations of the fields in the air gap can be written in a reference frame rotating with the rotor, which are shown in (2.3) and (2.4):

$$b_p(\theta',t) = \hat{B}_p cos((\omega_p - p_p\omega_m)t - p_p\theta' + \alpha_p) \tag{2.3}$$

$$b_c(\theta',t) = \hat{B}_c cos((\omega_c + p_c\omega_m)t + p_c\theta' + \alpha_c) \tag{2.4}$$

When the frequency and distribution of current induced by these two fields in the rotor are equal [4], two stator windings will be coupled through the rotor. The relationship of induced frequency between two stator windings is described in (2.5)

$$\omega_p - p_p\omega_m = \omega_c + p_c\omega_m = \omega_r \tag{2.5}$$

which gives (2.6):

$$\omega_m = \frac{\omega_p - \omega_c}{p_p + p_c} \tag{2.6}$$

In B-DFIG, there are two slips s_p and s_c and below some derivations are given.

At the side of PW, slip is shown in (2.7):

$$s_p = \frac{60f_p - p_p n}{60f_p} \tag{2.7}$$

At the side of rotor, the frequency of induced current is indicated in (2.8):

$$f_r = s_p f_p = \frac{60f_p - p_p n}{60} \tag{2.8}$$

At the side of CW, slip is written in (2.9):

$$s_c = \frac{60f_r - p_c n}{60f_r} = \frac{60s_p f_p - p_c n}{60s_p f_p} = \frac{60f_p - (p_p + p_c)n}{60f_p - p_p n} \tag{2.9}$$

The frequency of CW current is given in (2.10):

$$f_c = s_c f_r = \frac{60f_p - (p_p + p_c)n}{60f_p - p_p n} \times \frac{60f_p - p_p n}{60} = \frac{60f_p - (p_p + p_c)n}{60} \tag{2.10}$$

Transformations for (2.10) are shown in (2.11) and (2.12):

$$60f_c = 60f_p - (p_p + p_c)n \tag{2.11}$$

$$n = \frac{60f_p - 60f_c}{p_p + p_c} = 60 \times \frac{f_p - f_c}{p_p + p_c} \tag{2.12}$$

Through (2.11) and (2.12), the method to calculate the mechanical frequency of rotor can be got in (2.13), which corresponds to (2.6).

$$f_m = \frac{f_p - f_c}{p_p + p_c} \tag{2.13}$$

The slip s can be written in (2.14):

$$s = s_p s_c = \frac{f_r}{f_p} \times \frac{f_c}{f_r} = \frac{f_c}{f_p} \tag{2.14}$$

According to (2.6) and (2.13), when the frequency of CW current is positive, it means the fundamental field of CW is rotating in the opposite direction to that of PW. This operating mode is called *sub-synchronous* mode. When the frequency of CW current is negative, it means the fundamental field of CW is rotating in the same direction as that of PW. This operating mode is called *super-synchronous* mode. The rotating direction of winidings in B-DFIG is shown in Figure 2.7. In addition, in Figure 2.8, it has given the relationships of power in both PW and CW at different speed. In the ideal situation, the losses in B-DFIG are not taken into account. When B-DFIG runs at natural speed, CW neither absorbs nor delivers power and ω_c is zero. When ω_c is positive, it is in sub-synchronous mode and in this mode, CW absorbs power while PW delivers power. When ω_c is negative, B-DFIG runs in super-synchronous mode where both PW and CW generate electricity. In Figure 2.9, it has shown the relationship between electric torque and load angle. The load angle is defined by the phase difference between CW and PW current. From this figure, it can be observed that the produced electric torque of B-DFIG can be controlled by load torque, which is similar to a synchronous machine. When the load torque increase or decrease, B-DFIG can produce the enough electric torque to follow the load torque and keep the machine stable. However, if load torque increase too much, B-DFIG cannot produce enough electric torque. B-DFIG will run out of synchronism and enter the unstable region.

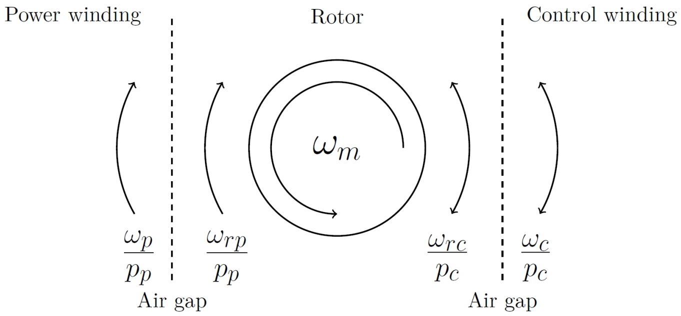

Figure 2.7: Rotating Direction of B-DFIG [5]

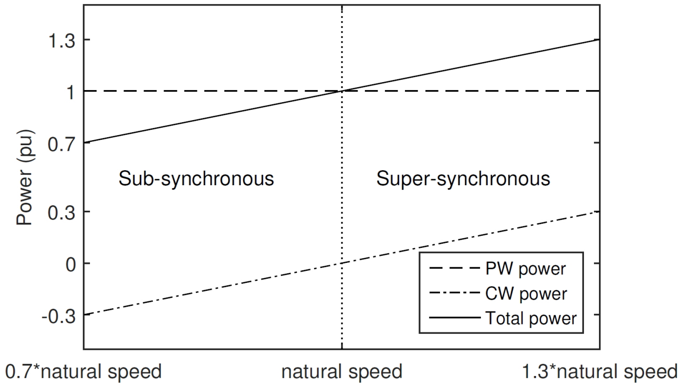

Figure 2.8: Speed Range of B-DFIG [5]

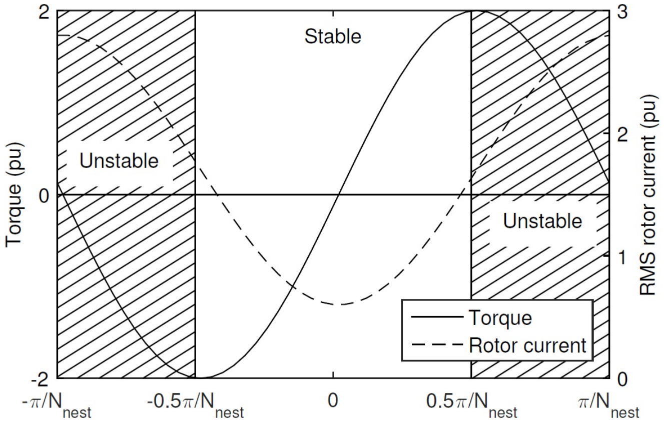

Figure 2.9: Torque-Load Angle Characteristic of B-DFIG [5]

2.3. STEADY STATE MODELING

IN steady state modeling, the common method is to build equivalent circuits for the machine. In this thesis, there are three kinds of equivalent circuits based on [6], which are equivalent, simplified equivalent and Γ-equivalent circuits. These three kinds of equivalent circuits have been presented step by step and they become simpler and simpler with the development of equivalent circuit.

2.3.1. EQUIVALENT CIRCUIT

To build equivalent circuit for B-DFIG, reasonable assumptions should be proposed first:

1. Saturation, eddy current and hysteresis should be neglected.

2. The rotor is cylindrical, the air gap is uniform, the surfaces of rotor and stator are so smooth that B-DFIG can neglect slotting effects.

3. The stator winding has a perfect sinusoidal distribution and the distribution of current is sinusoidal and balanced.

4. Between PW and CW, there is no coupling and mutual inductance.

B-DFIG has two stator windings (PW and CW) and one rotor winding and it is suitable for considering each stator winding has one resistance, one leakage inductance and one main inductance. Rotor winding couples with both PW and CW, hence it has two main inductance coupling with both PW and CW respectively. Figure 2.10 describes the equivalent circuit of B-DFIG proposed in [6] and the voltage equations are given in (2.15)-(2.20):

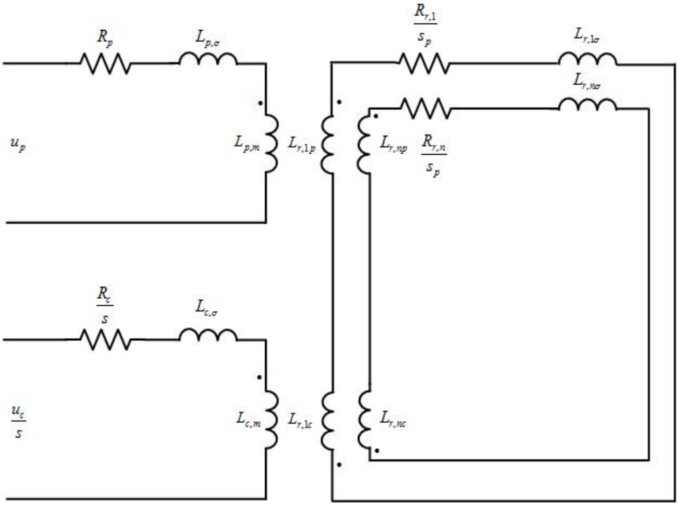

Figure 2.10: Single Phase Equivalent Circuit with n Rotor Loops [6]

$$\underline{U}_p = R_p\underline{I}_p + j\omega_p L_p \underline{I}_p + \sum_{n=1}^{N_l} j\omega_p M_{p,rn}\underline{I}_{r,n} \tag{2.15}$$

$$\frac{\underline{U}_c}{s} = \frac{R_c}{s}\underline{I}_c + j\omega_p L_c \underline{I}_c - \sum_{n=1}^{N_l} j\omega_p M_{c,rn}\underline{I}_{r,n} \tag{2.16}$$

$$0 = \frac{R_{r,n}}{s_p}\underline{I}_{r,n} + j\omega_p L_{r,n}\underline{I}_{r,n} + j\omega_p M_{p,rn}\underline{I}_p - j\omega_p M_{c,rn}\underline{I}_c \tag{2.17}$$

$$L_p = L_{p,\sigma} + L_{p,m} \tag{2.18}$$

$$L_c = L_{c,\sigma} + L_{c,m} \tag{2.19}$$

$$L_{r,n} = L_{r,n\sigma} + L_{r,np} + L_{r,nc} \tag{2.20}$$

In these equations, the component $\underline{X}$ represents a complex phasor component. In addition, s and s_p are given in section 2.2.3. To make all of frequencies can be used by ω_p in different windings, all of variables in CW and rotor part are converted into PW, hence there are factors s_p and s (s=$s_p s_c$) in rotor and CW respectively. M means the mutual inductance between PW and rotor, CW and rotor respectively.

In the equivalent circuit, parameters will be defined as follows:

1. Every rotor loop is identified by the index n and l in which n means the nest number and l means the loop number. The total number of loops is N_l and the total number of nests is N_n.

2. R_p represents the resistance in PW and R_c means the resistance in CW. $R_{r,n}$ is the resistance of rotor, in which n is from 1 to N_l.

3. Self inductance in PW and CW are L_p and L_c respectively, in which self inductance consists of main inductance and leakage inductance m and σ in subscript. However, for the self inductance of rotor, except leakage inductance $L_{r,n\sigma}$, there are two main inductance $L_{r,np}$ and $L_{r,nc}$, because both PW and CW are coupling with the rotor.

4. Mutual inductance between PW and the n^{th} rotor loop is $M_{p,rn}$ and that between CW and the n^{th} rotor loop is given by $M_{c,rn}$.

To simplify the equivalent circuit and voltage equations, every rotor can be assumed to contain only one loop. In that case, (2.15)-(2.17) will be transformed into (2.21)-(2.23):

$$\underline{U}_p = R_p \underline{I}_p + j\omega_p L_p \underline{I}_p + j\omega_p M_{p,r} \underline{I}_r \tag{2.21}$$

$$\frac{\underline{U}_c}{s} = \frac{R_c}{s} \underline{I}_c + j\omega_p L_c \underline{I}_c - j\omega_p M_{c,r} \underline{I}_r \tag{2.22}$$

$$0 = \frac{R_r}{s_p} \underline{I}_r + j\omega_p L_r \underline{I}_r + j\omega_p M_{p,r} \underline{I}_p - j\omega_p M_{c,r} \underline{I}_c \tag{2.23}$$

The single phase equivalent circuit with one rotor loop proposed in [6] is shown in Figure 2.11:

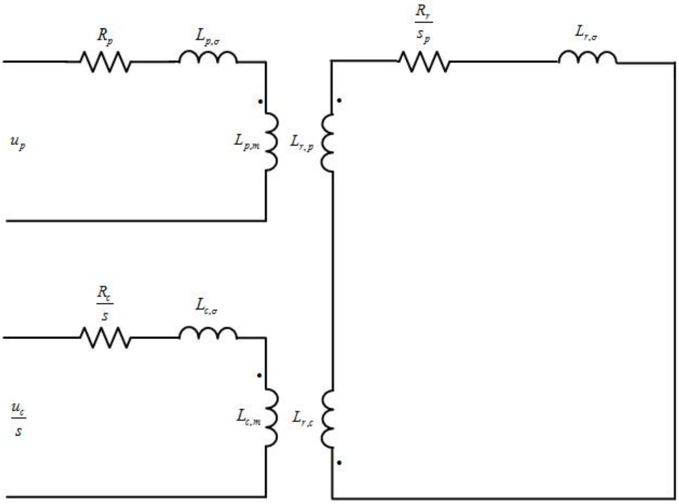

Figure 2.11: Single Phase Equivalent Circuit with One Rotor Loop [6]

2.3.2. SIMPLIFIED EQUIVALENT CIRCUIT

When the stator and rotor are transformed into a single circuit, a simplified equivalent circuit can be produced. In Figure 2.12, the simplified equivalent circuit proposed in [6] will be finished by first transforming CW circuit into rotor circuit. After that, in Figure 2.13, the rotor circuit should be transformed into PW circuit.

The first procedure is transforming CW into rotor and the transformation ratio is displayed in (2.24):

$$\frac{L_{c,m}}{L_{r,c}} = a \tag{2.24}$$

Figure 2.12 describes the transformation and the parameters are shown in (2.25)-(2.27):

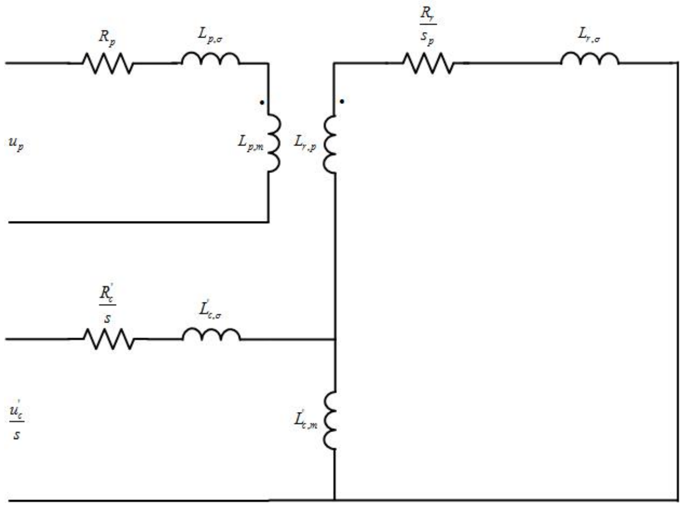

Figure 2.12: First Step in the Simplified Equivalent Circuit Formation [6]

$$R_c' = \frac{1}{a} R_c \tag{2.25}$$

$$L_{c,\sigma}' = \frac{1}{a} L_{c,\sigma} \tag{2.26}$$

$$L_{c,m}' = L_{r,c} \tag{2.27}$$

The next procedure is transforming this circuit into PW circuit and the transformation ratio is shown in (2.28):

$$\frac{L_{p,m}}{L_{r,p}} = b \tag{2.28}$$

Figure 2.13 indicates the simplified equivalent circuit proposed in [6] and the parameters are written in (2.29)-(2.33):

$$R''_c = bR'_c = \frac{b}{a}R_c \tag{2.29}$$

$$L''_{c,\sigma} = bL'_{c,\sigma} = \frac{b}{a}L_{c,\sigma} \tag{2.30}$$

$$L''_{c,m} = bL'_{c,m} = bL_{r,c} \tag{2.31}$$

$$R'_r = bR_r \tag{2.32}$$

$$L'_{r,\sigma} = bL_{r,\sigma} \tag{2.33}$$

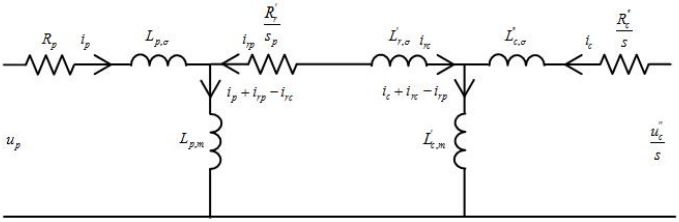

Figure 2.13: Simplified Equivalent Circuit [6]

In addition, voltage equations of PW, CW and rotor part are shown in (2.34)-(2.37):

$$\underline{U}_p = R_p\underline{I}_p + j\omega_p L_{p,\sigma}\underline{I}_p + j\omega_p L_{p,m}(\underline{I}_p + \underline{I}_r) \tag{2.34}$$

$$\frac{\underline{U}''_c}{s} = \frac{R''_c}{s}\underline{I}_c + j\omega_p L''_{c,\sigma}\underline{I}_c + j\omega_p L'_{c,m}(\underline{I}_c - \underline{I}_r) \tag{2.35}$$

$$0 = j\omega_p L_{p,m}(\underline{I}_p + \underline{I}_r) - j\omega_p L'_{c,m}(\underline{I}_c - \underline{I}_r) + j\omega_p L'_{r,\sigma}\underline{I}_r + \frac{R'_r}{s_p}\underline{I}_r \tag{2.36}$$

$$\underline{I}_r = \underline{I}_{rp} - \underline{I}_{rc} \tag{2.37}$$

2.3.3. THE Γ-EQUIVALENT CIRCUIT

The Γ-equivalent circuit is another simplified equivalent circuit where the leakage inductance in both PW and CW is transformed into the main inductance of PW and CW and the leakage inductance of the rotor. In this consideration, PW and CW do not have any leakage inductance, which is simpler than normal simplified equivalent circuit. Some parameters [7] in (2.34)-(2.36) are derived in (2.38)-(2.41):

$$L_{pm,\gamma} = L_{p,\sigma} + L_{p,m} \tag{2.38}$$

$$L'_{cm,\gamma} = L''_{c,\sigma} + L'_{c,m} \tag{2.39}$$

$$L'_{r\sigma,\gamma} = c^2 d^2 L'_{r,\sigma} + cL_{p,\sigma} + dL''_{c,\sigma} \tag{2.40}$$

$$R''_r = c^2 d^2 R'_r \tag{2.41}$$

in which, the expression of c and d are shown in (2.42) and (2.43):

$$c = \frac{L_{p,\sigma} + L_{p,m}}{L_{p,m}} \tag{2.42}$$

$$d = \frac{L''_{c,\sigma} + L'_{c,m}}{L'_{c,m}} \tag{2.43}$$

Through some transformations, (2.44)-(2.47) describe the relationship between parameters which have been calculated from (2.38)-(2.41) in Γ-equivalent circuit.

$$\underline{U}_p = R_p \underline{I}_p + j\omega_p L_{pm,\gamma}(\underline{I}_p + \underline{I}'_r) \tag{2.44}$$

$$\frac{\underline{U}''_c}{s} = \frac{R''_c}{s}\underline{I}_c + j\omega_p L'_{cm,\gamma}(\underline{I}_c - \underline{I}'_r) \tag{2.45}$$

$$0 = j\omega_p L_{pm,\gamma}(\underline{I}_p + \underline{I}'_r) - j\omega_p L'_{cm,\gamma}(\underline{I}'_c - \underline{I}_r) + j\omega_p L'_{r\sigma,\gamma}\underline{I}'_r + \frac{R''_r}{s_p}\underline{I}'_r \tag{2.46}$$

$$\underline{I}'_r = \underline{I}'_{rp} - \underline{I}'_{rc} \tag{2.47}$$

Through above procedures, Γ-equivalent circuit proposed in [8] can be derived, which is displayed in Figure 2.14:

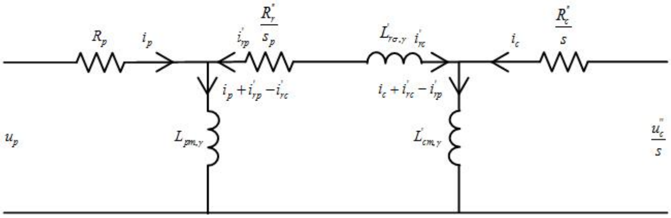

Figure 2.14: Γ-Equivalent Circuit [8]

When ignoring the stator magnetizing inductance and the stator and rotor resistance, an inner core model proposed in [9] will be derived for the equivalent circuit of the machine, which is displayed in Figure 2.15. B-DFIG has a relative large leakage inductance which cannot be omitted [8]. The circuit is similar with a synchronous machine ignoring stator resistance, because the angle between CW voltage and PW voltage can be changed to produce different torque, active power and reactive power. The difference between the inner core model of B-DFIG and synchronous machine is that the excitation part in B-DFIG is induced by CW while in synchronous machine, that is induced by rotor.

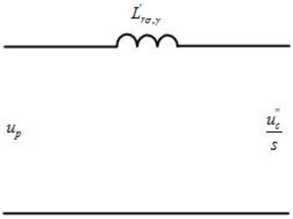

Figure 2.15: Inner Core Equivalent Circuit [9]

2.4. SUMMARY

THE operating principles of B-DFIG have been introduced in this chapter clearly first. Through three different kinds of operating modes, this machine can be understood better. Actually, both simple and cascade modes are called asynchronous modes which are not usually used in industry. In addition, through some measurement results in experiment, it can be seen that in these two modes, B-DFIG behaves like an induction machine. For the synchronous mode, there are many advantages and the machine is easily controlled by control strategy in the power electronic converter. Therefore, that is the most popular mode of operation. Moreover, some equations between different variables have been given to understand the theory of B-DFIG better.

After that, the steady state modeling for the machine has been finished in this chapter, which starts from normal equivalent circuit with single rotor loop and multiple rotor loops. Then by using a transformation ratio, the simplified equivalent circuit substitutes the normal equivalent circuit because both stator and rotor windings have been transformed into one circuit. Next, through some calculations in new parameters, Γ-equivalent circuit is derived. It is worth noting that in Γ-equivalent circuit, there is not any leakage inductance in both PW and CW because $L_{p,\sigma}$ and $L''_{c,\sigma}$ have been converted into rotor winding. $L_{pm,\gamma}$, $L'_{cm,\gamma}$ and $L'_{r\sigma,\gamma}$ contain the components of $L_{p,\sigma}$ and $L''_{c,\sigma}$ respectively. Via these three different kinds of equivalent circuits, the B-DFIG has been modelled in steady state completely, which is meaningful for dynamic modeling of B-DFIG in Chapter 3.

REFERENCES

[1] P. C. Roberts, *A study of brushless doubly-fed (induction) machines,* (2005).

[2] S. Tohidi, H. Oraee, M. R. Zolghadri, S. Shao, and P. Tavner, *Analysis and enhance-*

ment of low-voltage ride-through capability of brushless doubly fed induction generator, IEEE Transactions on Industrial Electronics **60**, 1146 (2013).

[3] T. Strous, *Brushless doubly fed induction machines for wind turbine drive-train applications,* (2016).

[4] S. Williamson, A. Ferreira, and A. Wallace, *Generalised theory of the brushless doubly-fed machine. part 1: Analysis,* IEE Proceedings-Electric Power Applications **144**, 111 (1997).

[5] X. Wang, *Modeling and design of brushless doubly-fed induction machines,* (2017).

[6] U. Shipurkar, *Brushless doubly fed induction generator based wind turbine drivetrain under grid fault conditions,* (2014).

[7] G. R. SLEMON, *Circuit models for polyphase induction machines,* Electric machines and power systems **8**, 369 (1983).

[8] P. Roberts, R. McMahon, P. Tavner, J. Maciejowski, and T. Flack, *Equivalent circuit for the brushless doubly fed machine (bdfm) including parameter estimation and experimental verification,* IEE Proceedings-Electric Power Applications **152**, 933 (2005).

[9] R. McMahon, P. Roberts, X. Wang, and P. Tavner, *Performance of bdfm as generator and motor,* IEE Proceedings-Electric Power Applications **153**, 289 (2006).

3

B-DFIG DYNAMIC MODEL

3.1. INTRODUCTION

TO build a B-DFIG model and observe its behaviours in both transient state and steady state, it is necessary to derive its differential equations and to build its dynamic model. Firstly, differential equations are derived to express the relationship between variables in transient state. Then block diagrams are built to form a B-DFIG model.

3.2. DIFFERENTIAL EQUATIONS

DURING the low voltage dip condition in the grid, the reaction of machine belongs to the dynamic domain. Therefore, it is necessary to build a dynamic model for B-DFIG. B-DFIG can be represented by dynamic equivalent circuit where it is possible to derive differential equations for the machine to describe the time-dynamic relations. In [1], dynamic equivalent circuit is given, which is shown in Figure 3.1. In this equivalent circuit, the concept of Ideal Rotating Transformer (IRTF) is introduced [2][3]. IRTF can represent the energy exchange between stator, rotor and mechanical part. In addition, it shows the transformation of space-vector from one coordinate system to another one due to the position change of rotor. This figure is similar to Figure 2.2, in which both of transformation ratios between PW and rotor and rotor and CW are converted into PW and all of leakage inductance is transformed into CW.

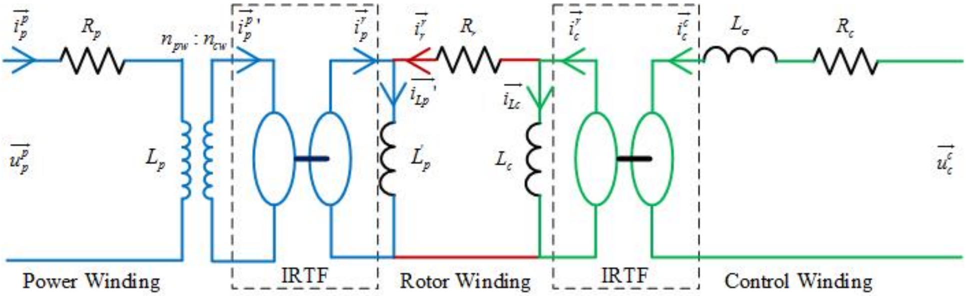

Figure 3.1: Equivalent Circuit of B-DFIG [1]

According to the equivalent circuit, some differential equations can be derived which are shown in (3.1)-(3.7):

Power Winding System:

$$\frac{d\vec{\lambda}_p^p}{dt} = (\vec{u}_p^p - R_p\vec{i}_p^p)\frac{n_{cw}}{n_{pw}} \tag{3.1}$$

$$\vec{i}_p'^p \frac{n_{cw}}{n_{pw}} = \vec{i}_p^p \tag{3.2}$$

Rotor System:

$$\vec{\lambda}_p^r = (\vec{i}_p^r + \vec{i}_r^r)L_p' \tag{3.3}$$

$$\frac{d\vec{\lambda}_R}{dt} = R_r\vec{i}_r^r \tag{3.4}$$

$$\vec{\lambda}_p^r + \vec{\lambda}_R = \vec{\lambda}_c^r \tag{3.5}$$

$$\vec{\lambda}_c^r = (\vec{i}_c^r - \vec{i}_r^r)L_c \tag{3.6}$$

Control Winding System:

$$\frac{d\vec{\lambda}_c^c}{dt} = \vec{u}_c^c - R_c\vec{i}_c^c - L_\sigma\frac{d\vec{i}_c^c}{dt} \tag{3.7}$$

Through these differential equations, the block diagram can be built, which are suitable for numerical integration. However, saturation effects, time and space harmonic distortions are not taken into account. It is assumed that windings are symmetrically balanced and sinusoidally distributed.

3.3. Block Diagram

According to differential equations written in section 3.2, block diagrams proposed in [1] can be presented in Figure 3.2. In this figure, there are three fundamental electrical sections: power-winding section, control-winding section and rotor-winding section in a nested-loop construction.

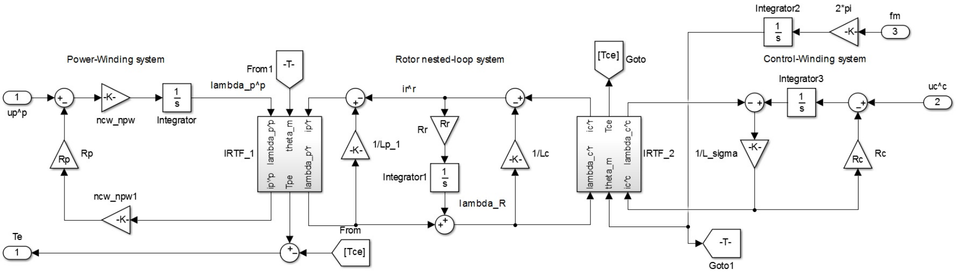

Figure 3.2: B-DFIG Time Dynamic Model

By applying Clarke's transformation, every part can be transformed into an equivalent model with two orthogonal windings, which can use space-vector formulations. Therefore, all of electrical components like voltage u, current i and flux linkage λ will be shown as space-vectors in various orthogonal coordinate systems.

Every part in the equivalent circuit is modelled in its own coordinate system, hence a series of equations can be more straightforward than general model using a unified reference frame [4][5]. In Figure 3.1, ^{p} and ^{c} represent PW and CW coordinate system respectively, as a result of vector components rotating with PW and CW frequency. ^{r} means the rotor coordinate system, leading vector components rotating with rotor frequency f_r. In (3.4) and (3.5), λ_R means lost flux on the rotor resistance.

With the change of mechanical rotor position angle θ_m, a space-vector from PW or CW coordinate system rotates with a same frequency when converted into the rotor coordinate system. The frequency f_r is shown in (3.8):

$$f_r = f_p - p_p f_m = f_c + p_c f_m \tag{3.8}$$

Different coordinate systems are shown in Figure 3.3. Transformation of space-vectors from one coordinate system to another one is achieved by using a rotational transformation which are shown in (3.9) and (3.10):

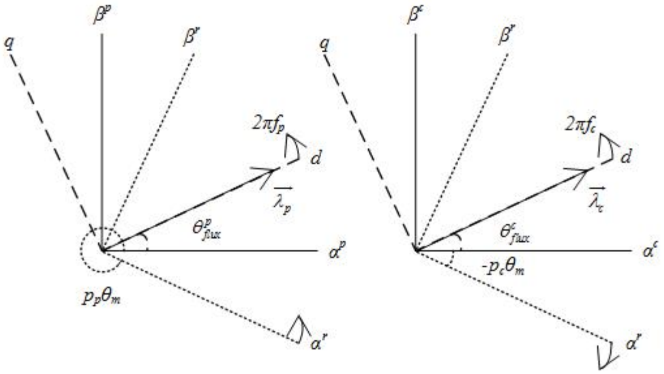

Figure 3.3: Vector Coordinate System

$$\vec{i}_p^r = C_{rot}(-p_p\theta_m)\vec{i}_p^p \tag{3.9}$$

$$\vec{i}_c^r = C_{rot}(p_c\theta_m)\vec{i}_c^c \tag{3.10}$$

in which, C_{rot} is described in (3.11):

$$C_{rot}(\theta) = \begin{bmatrix} cos(\theta) & -sin(\theta) \\ sin(\theta) & cos(\theta) \end{bmatrix} \tag{3.11}$$

Power and Torque [6]

In B-DFIG, electrical and mechanical energy exchange happens in magnetic field between stator and rotor circuits. The total electric power absorbed by the stator winding is in (3.12):

$$p_s = u_{sa}i_{sa} + u_{sb}i_{sb} + u_{sc}i_{sc} = \vec{u}^T_{sabc}\vec{i}_{sabc} \tag{3.12}$$

When applying Clarke's Transformation (power invariant), (3.12) is transformed into (3.13):

$$\begin{aligned} p_s &= (C^{-1}_{\alpha\beta0,abc}\vec{u}_{s\alpha\beta0})^T(C^{-1}_{\alpha\beta0,abc}\vec{i}_{s\alpha\beta0}) = \vec{u}^T_{s\alpha\beta0}(C^{-1}_{\alpha\beta0,abc})^T C^{-1}_{\alpha\beta0,abc}\vec{i}_{s\alpha\beta0} = \vec{u}^T_{s\alpha\beta0}\vec{i}_{s\alpha\beta0} \\ &= u_{s\alpha}i_{s\alpha} + u_{s\beta}i_{s\beta} + u_{s0}i_{s0} \end{aligned} \tag{3.13}$$

Clarke's Transformation is shown in (3.14):

$$C_{\alpha\beta0,abc} = \sqrt{\frac{2}{3}}\begin{bmatrix} 1 & -\frac{1}{2} & -\frac{1}{2} \\ 0 & \frac{\sqrt{3}}{2} & -\frac{\sqrt{3}}{2} \\ \frac{1}{\sqrt{2}} & \frac{1}{\sqrt{2}} & \frac{1}{\sqrt{2}} \end{bmatrix} \tag{3.14}$$

For a variable X, it can mean a vector $[X_\alpha\ X_\beta]^T$ in transient state and also can represent a phasor $X = X_\alpha + jX_\beta$ in steady state. Therefore, in steady state, the apparent power, active power and reactive power of stator winding can be expressed in (3.15)-(3.17):

$$S = \underline{u}_s \overline{\underline{i}}_s \tag{3.15}$$

$$P = Re[\underline{u}_s \overline{\underline{i}}_s] \tag{3.16}$$

$$Q = Im[\underline{u}_s \overline{\underline{i}}_s] \tag{3.17}$$

The zero components of variables in stator winding are zero in this chapter, hence the expression of active power and reactive power can be derived in (3.18) and (3.19):

$$P = u_{s\alpha} i_{s\alpha} + u_{s\beta} i_{s\beta} = \vec{u}_s^T \vec{i}_s = \vec{i}_s^T \vec{u}_s \tag{3.18}$$

$$Q = u_{s\beta} i_{s\alpha} - u_{s\alpha} i_{s\beta} = \vec{u}_s^T \begin{bmatrix} 0 & -1 \\ 1 & 0 \end{bmatrix} \vec{i}_s = \vec{i}_s^T \begin{bmatrix} 0 & 1 \\ -1 & 0 \end{bmatrix} \vec{u}_s \tag{3.19}$$

(3.20) describes the relationship between vector $\vec{X}_s$ and the α-β components of vector $\vec{X}_s$: $[X_\alpha\ X_\beta]^T$:

$$\begin{bmatrix} X_{s\alpha} \\ X_{s\beta} \end{bmatrix} = X_s \begin{bmatrix} cos(p\theta) \\ sin(p\theta) \end{bmatrix} \tag{3.20}$$

The derivative of the α and β components of vector $\vec{X}_s$ is shown in (3.21):

$$d\begin{bmatrix} X_{s\alpha} \\ X_{s\beta} \end{bmatrix} = X_s \begin{bmatrix} -sin(p\theta) \\ cos(p\theta) \end{bmatrix} pd\theta = \begin{bmatrix} -X_{s\beta} \\ X_{s\alpha} \end{bmatrix} pd\theta = \begin{bmatrix} 0 & -1 \\ 1 & 0 \end{bmatrix} \begin{bmatrix} X_{s\alpha} \\ X_{s\beta} \end{bmatrix} pd\theta \tag{3.21}$$

The expression of stator voltage is displayed in (3.22):

$$\begin{aligned} \vec{u}_s &= R_s \vec{i}_s + \frac{d\vec{\lambda}_{s\sigma}}{dt} + \frac{d\vec{\lambda}_{sm}}{dt} = R_s \vec{i}_s + L_{s\sigma} \frac{d\vec{i}_s}{dt} + \frac{\vec{\lambda}_{sm}}{dt} \\ &= R_s \vec{i}_s + L_{s\sigma} \begin{bmatrix} 0 & -1 \\ 1 & 0 \end{bmatrix} \vec{i}_s p \frac{d\theta}{dt} + \begin{bmatrix} 0 & -1 \\ 1 & 0 \end{bmatrix} \vec{\lambda}_{sm} p \frac{d\theta}{dt} \end{aligned} \tag{3.22}$$

In that case, (3.18) is transformed into (3.23):

$$\begin{aligned} p_s &= \vec{i}_s^T \vec{u}_s \\ &= R_s \vec{i}_s^T \vec{i}_s + L_{s\sigma} \vec{i}_s^T \begin{bmatrix} 0 & -1 \\ 1 & 0 \end{bmatrix} \vec{i}_s p \frac{d\theta}{dt} + \vec{i}_s^T \begin{bmatrix} 0 & -1 \\ 1 & 0 \end{bmatrix} \vec{\lambda}_{sm} p \frac{d\theta}{dt} \end{aligned} \tag{3.23}$$

The first item is the copper loss in the stator winding and the second item is the energy stored in the magnetic field, hence the third item is the electric power. The relationship between electric power and torque is written in (3.24):

$$p_{em} = T_e \frac{d\theta}{dt} \tag{3.24}$$

Torque T_{pe} and T_{ce} produced by PW and CW can be derived in (3.25) and (3.26):

$$T_{pe} = p_p \vec{i}_p^{rT} \begin{bmatrix} 0 & -1 \\ 1 & 0 \end{bmatrix} \vec{\lambda}_p^r \tag{3.25}$$

$$T_{ce} = p_c \vec{i}_c^{rT} \begin{bmatrix} 0 & -1 \\ 1 & 0 \end{bmatrix} \vec{\lambda}_c^r \tag{3.26}$$

The electric torque T_e produced by B-DFIG is given in (3.27):

$$T_e = T_{pe} - T_{ce} \tag{3.27}$$

Mechanical System

The relationship between mechanical position angle, angular velocity and mechanical frequency is displayed in (3.28):

$$\frac{d\theta_m}{dt} = \omega_m = 2\pi f_m \tag{3.28}$$

In reality, the shaft of B-DFIG rotor is connected to the load (wind) and different speed levels will be taken under various speed of wind. The relationship between speed and load torque is described in (3.29):

$$T_e - T_l = J \frac{d\omega}{dt} \tag{3.29}$$

According to (3.29), mechanical system can be produced in Figure 3.4:

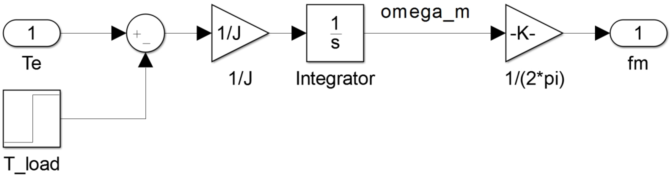

Figure 3.4: Mechanical System

Now, the series of differential equations ((3.1)-(3.7), (3.9)-(3.11), (3.25)-(3.29)) are transformed into a block diagram which is shown in Simulink (Matlab) software. There are two electrical input ports for flux and current, a mechanical input port for mechanical position angle in IRTF. The expression of the rotational transformation is in (3.11) and Figure 3.2 shows the time dynamic model of B-DFIG in block diagram developed in Simulink. The strength of this model is that all of electrical components are modelled and simulated in their own stationary reference frame, which also reduces the necessity for additional reference transformations.

3.4. SUMMARY

THE dynamic model of B-DFIG has been described in this chapter. Firstly, some differential equations are derived, which are suitable for describing this machine. Having introduced the IRTF, all of the space vectors can be transformed into the same reference frame. Then, block diagram is built based on these differential equations. After that, the control strategy should be added to the power electronic converter of the machine to make B-DFIG model completely, which will be elaborated in Chapter 4.

REFERENCES

[1] T. Strous, *Brushless doubly fed induction machines for wind turbine drive-train applications,* (2016).

[2] A. V. P. Van den Bosch, *A universal method for modelling electrical machines,* .

[3] R. De Doncker, D. W. Pulle, and A. Veltman, *Advanced electrical drives: analysis, modeling, control* (Springer Science & Business Media, 2010).

[4] J. Poza, E. Oyarbide, D. Roye, and M. Rodriguez, *Unified reference frame dq model of the brushless doubly fed machine,* IEE Proceedings-Electric Power Applications **153**, 726 (2006).

[5] F. Barati, S. Shao, E. Abdi, H. Oraee, and R. McMahon, *Generalized vector model for the brushless doubly-fed machine with a nested-loop rotor,* IEEE Transactions on Industrial Electronics **58**, 2313 (2011).

[6] M. Hoeijmakers, *Modelling of ac machines,* Delft University of Technology, Delft, The Netherlands (2004).

4

B-DFIG CONTROL STRATEGY

4.1. INTRODUCTION

THE dynamic model of B-DFIG has been built in Chapter 3. In the next step, the control strategy is applied to B-DFIG to ensure it operates at synchronous mode. A power electronic converter is added to the previous model and basic simulations are done to certify the feasibility of the controller.

4.2. CONTROL STRATEGY

THERE are many different kinds of control strategies which have been implemented on B-DFIG, including open-loop scalar control, close-loop scalar control [1][2], phase angle control [3], indirect stator quantities control [4–6] and vector control [7–9]. For the vector control, there are two popular vector control schemes called Voltage Oriented Control (VOC) and Field Oriented Control (FOC). VOC is regarding voltage as a reference frame which is always used in active and reactive power control while FOC is taking the flux as the main reference frame which can be developed in the speed and torque control. The difference between VOC and FOC is that in FOC, it provides the decoupling control of active power (torque) and reactive power (flux) while it needs angle estimation and machine parameters identification (R_r and L_σ). However, in VOC, it only can control the active power directly and does not need any parameters of the machine, hence it is more robust than FOC [10]. FOC provides better dynamic performance and also has been widely developed in conventional DFIG drive systems [11][12] and in the implementation of sensorless DFIG control scheme [13–15]. FOC schemes have been applied in the experiment of B-DFIG [16–19] but the development and implementation of the sensorless contorl strategy is proved to be more difficult.

A fully functional sensorless control strategy proposed in [20] is presented in this section for the B-DFIG based on FOC. Sensorless means it does not require real mechanical position, which increases the reliability and cost effectiveness of B-DFIG.

A complete B-DFIG model contains the machine's model and the controller used to control the behavior of B-DFIG in a stable and responsive manner. Figure 4.1 describes the development of the complete B-DFIG model proposed in [20] in Simulink:

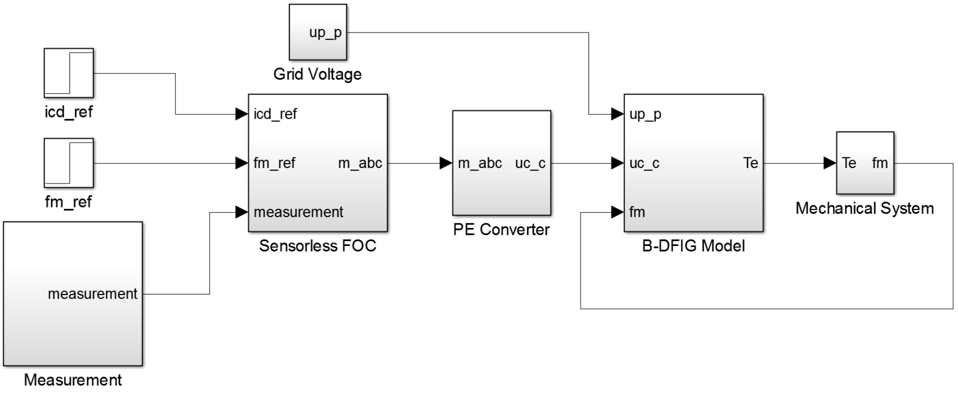

Figure 4.1: Complete B-DFIG Model

In this complete model, it consists of not only machine's model, but also grid voltage side, sensorless FOC, power electronic converter, measurement block and mechanical system. For the reference signal, there are two items. One is f_m reference signal to control the mechanical speed and the other is i_{cd} reference signal to control the magnetizing current.

4.2.1. SENSORLESS FIELD ORIENTED CONTROL

For the most important part in the controller is Sensorless FOC block. Figure 4.2 describes the structure of sensorless FOC strategy proposed in [20] in details:

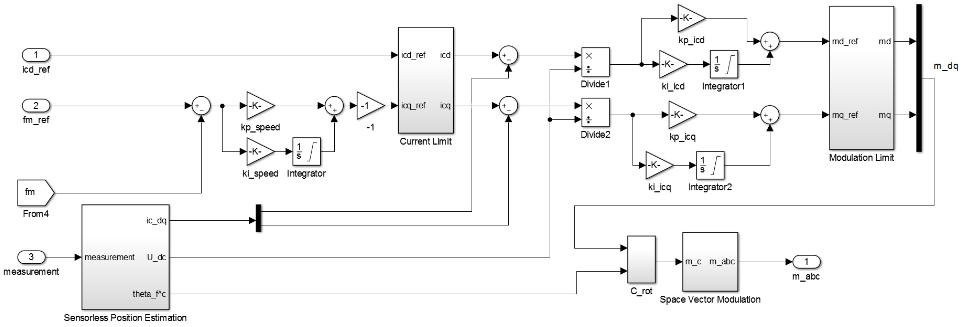

Figure 4.2: Sensorless FOC Strategy

There are two control loops in the sensorless FOC strategy. The inner loop is PI current loop controlling the current vector $\vec{i}_c^{dq}$ in CW flux coordinate system. In that case, the current vector becomes DC values and gets rid of the fundamental frequency of CW current. The transformations between two vectors are shown in (4.1)-(4.3):

$$\vec{u}_c^{dq} = C_{rot}(-\theta^c_{flux})\vec{u}_c^c \tag{4.1}$$

$$\vec{i}_c^{dq} = C_{rot}(-\theta^c_{flux})\vec{i}_c^c \tag{4.2}$$

$$\vec{\lambda}_c^{dq} = C_{rot}(-\theta^c_{flux})\vec{\lambda}_c^c = \begin{bmatrix} |\vec{\lambda}_c^c| \\ 0 \end{bmatrix} \tag{4.3}$$

In (4.1)-(4.3), θ^c_{flux} is the flux position angle which can be achieved in the Sensorless Position Estimation block. In B-DFIG model, $\vec{\lambda}_c^c$ (in $\alpha-\beta$ coordinate system) has been achieved. Further, flux position angle is displayed in (4.4):

$$\theta^c_{flux} = arctan(\frac{\lambda_{c\beta}}{\lambda_{c\alpha}}) \tag{4.4}$$

Torque is controlled by q-axis CW current i_{cq} because in this B-DFIG model, all of the leakage inductance is converted into CW. According to (3.3) and (3.6), the relationship between PW current and CW current can be written in (4.5):

$$i_c^r = -i_p^r + \frac{\lambda_c^r}{L_c} + \frac{\lambda_p^r}{L_p'} \tag{4.5}$$

When converting all of the variables into CW reference frame, (4.5) will be divided into (4.6) and (4.7):

$$i_{cd} = -\frac{n_{pw}}{n_{cw}} i_{pd} + \frac{|\lambda_c|}{L_c} + \frac{|\lambda_p|}{L_p'} \tag{4.6}$$

$$i_{cq} = -\frac{n_{pw}}{n_{cw}} i_{pq} \tag{4.7}$$

In (4.7), it can be seen that the q-axis PW current i_{pq} is proportional to the q-axis CW current i_{cq}. According to (3.25)-(3.27), (4.3) and (4.7), the expression of electric torque can be derived, which is written in (4.8). In this equation, the electric torque T_e is proportional to q-axis CW current i_{cq} without the influence of cross-coupling effect, which is the reason why the choice of dq-axis should be based on the CW flux reference frame (to make sure $\lambda_{cd} = |\lambda_c|$ and $\lambda_{cq} = 0$).

$$\begin{aligned} T_e &= p_p(i_{pq}\lambda_{pd} - i_{pd}\lambda_{pq}) - p_c(i_{cq}\lambda_{cd} - i_{cd}\lambda_{cq}) = p_p i_{pq}\lambda_{pd} - p_c i_{cq}\lambda_{cd} \\ &= -(\frac{n_{cw}}{n_{pw}} p_p\lambda_{pd} + p_c\lambda_{cd}) i_{cq} \end{aligned} \tag{4.8}$$

d-axis CW current i_{cd} controls the magnetizing current in CW, which is related to the flow of reactive power on both PW and CW. The output of the current control loop is the reference CW voltage signal, which should be scaled down by the dc-link U_{dc}. The result is the modulation index signal $\vec{m}^{dq}$. This signal should be limited between $\pm\frac{2}{\sqrt{3}}$, because the third harmonic will be injected to increase the voltage utilization and the amplitude of fundamental field of saddle modulation wave is $\frac{2}{\sqrt{3}}$ times larger than the amplitude of fundamental field of sinusoidal modulation wave. In front of PI current controller, there is a PI speed controller to control the mechanical speed. The speed is related to active power, so the output of PI speed controller is i_{cq} reference signal. In this thesis, the convention is that when the field of CW rotates in a different direction from that of PW, the frequency in CW is positive and when the field of CW rotates in a same direction as that of PW, the frequency in CW is negative. However, the rotating direction of rotor is the same as that of PW field. Therefore, there is a gain -1 between the output of PI speed controller and i_{cq} reference signal. To keep the dq-axis CW current in a limited value, there is a current limit between the output of PI speed controller and the input of PI current controller. Therefore, as Figure 4.2 shows, there are one current limit and one modulation limit in sensorless FOC. To control B-DFIG in a stable manner, a constant flux should be kept in the machine because the response time of d-axis components is an order of magnitude slower than q-axis value. When the reference values reach the limit, the magnetic field should be maintained first. Therefore, the d-axis values (current and modulation index) take precedence over the q-axis components, which can be achieved in the current limit and modulation limit. Figure 4.3 and 4.4 indicate the current limit and modulation limit which realize the requirement through dynamic saturation blocks:

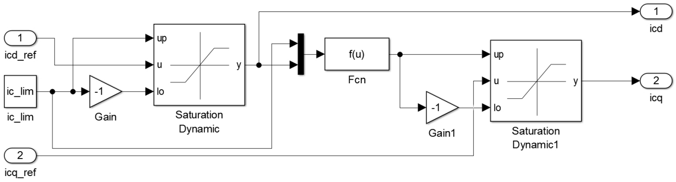

Figure 4.3: Current Limit

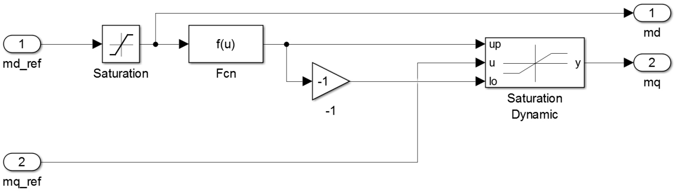

Figure 4.4: Modulation Limit

The response time of speed loop and current loop depend on the mechanical time constant and electrical time constant respectively. The mechanical time constant of an electrical machine is far outweigh the electrical time constant, hence the inner loop is an order of magnitude faster than the outer loop. Therefore, in some other control applications, a PI speed controller can be neglected and the current control is sufficient.

4.2.2. SPACE VECTOR MODULATION

The space vector is developed by a three-phase inverter proposed in [21] which is shown in Figure 4.5. The input of this modulator is an average voltage reference signal and a series of switch control strategies act on these switches. All of these 6 switches can be divided into 3 groups. S_1 and S_4 belong to the first group S_a. Group S_b contains S_3 and S_6. S_5 and S_2 are in group S_c.

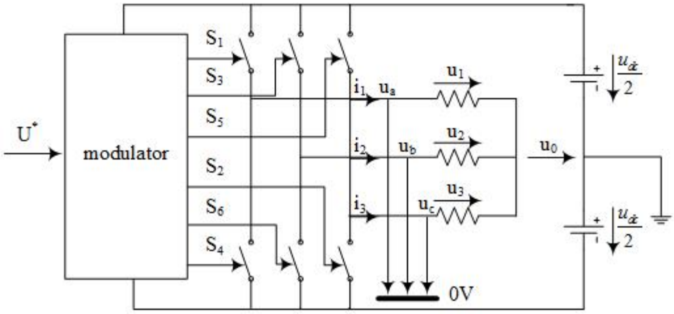

Figure 4.5: Three-Phase Inverter [21]

The relationship between average voltage reference signal and three-phase load voltage is given in (4.9):

$$\vec{U}^* = \begin{bmatrix} U_\alpha^* \\ U_\beta^* \end{bmatrix} = \sqrt{\frac{2}{3}} \begin{bmatrix} 1 & -\frac{1}{2} & -\frac{1}{2} \\ 0 & \frac{\sqrt{3}}{2} & -\frac{\sqrt{3}}{2} \end{bmatrix} \begin{bmatrix} U_1^* \\ U_2^* \\ U_3^* \end{bmatrix} \tag{4.9}$$

The three-phase load average voltage in each sample can be written in (4.10)-(4.16):

$$U_a(t_k) = \frac{1}{T_S} \int_{t_k}^{t_k+T_s} u_a(t)dt \tag{4.10}$$

$$U_b(t_k) = \frac{1}{T_S} \int_{t_k}^{t_k+T_s} u_b(t)dt \tag{4.11}$$

$$U_c(t_k) = \frac{1}{T_S} \int_{t_k}^{t_k+T_s} u_c(t)dt \tag{4.12}$$

$$U_0(t_k) = \frac{1}{T_s} \int_{t_k}^{t_k+T_s} u_0(t)dt \tag{4.13}$$

$$U_1^*(t_k) = U_a(t_k) - U_0(t_k) \tag{4.14}$$

$$U_2^*(t_k) = U_b(t_k) - U_0(t_k) \tag{4.15}$$

$$U_3^*(t_k) = U_c(t_k) - U_0(t_k) \tag{4.16}$$

in which $U_a(t_k)$, $U_b(t_k)$ and $U_c(t_k)$ mean three half-bridge average phase voltage. In addition, the required values of three half-bridge average phase voltage can be written in (4.17)-(4.19) with the aid of user defined three-phase load average voltage reference signal $U_1^*(t_k)$, $U_2^*(t_k)$ and $U_3^*(t_k)$.

$$U_a^*(t_k) = U_1^*(t_k) + U_0^*(t_k) \tag{4.17}$$

$$U_b^*(t_k) = U_2^*(t_k) + U_0^*(t_k) \tag{4.18}$$

$$U_c^*(t_k) = U_3^*(t_k) + U_0^*(t_k) \tag{4.19}$$

Therefore, with the aid of (4.17)-(4.19), (4.9) is transformed into (4.20):

$$\vec{U}^* = \begin{bmatrix} U_\alpha^* \\ U_\beta^* \end{bmatrix} = \sqrt{\frac{2}{3}} \begin{bmatrix} 1 & -\frac{1}{2} & -\frac{1}{2} \\ 0 & \frac{\sqrt{3}}{2} & -\frac{\sqrt{3}}{2} \end{bmatrix} \begin{bmatrix} U_a^* \\ U_b^* \\ U_c^* \end{bmatrix} - \sqrt{\frac{2}{3}} U_0^* \begin{bmatrix} 1 & -\frac{1}{2} & -\frac{1}{2} \\ 0 & \frac{\sqrt{3}}{2} & -\frac{\sqrt{3}}{2} \end{bmatrix} \begin{bmatrix} 1 \\ 1 \\ 1 \end{bmatrix} \tag{4.20}$$

the second item of the right side of (4.20) is zero and U_0^* means the zero sequence of average voltage. Therefore, it is chosen freely without affecting the average voltage reference signal. To make the maximum and minimum values of three half-bridges be symmetrical with time axis, (4.21) can be given:

$$max\{U_a^*(t_k), U_b^*(t_k), U_c^*(t_k)\} + min\{U_a^*(t_k), U_b^*(t_k), U_c^*(t_k)\} = 0 \tag{4.21}$$

With the help of (4.17)-(4.19), this expression can also be transformed into (4.22):

$$max\{U_1^*(t_k), U_2^*(t_k), U_3^*(t_k)\} + min\{U_1^*(t_k), U_2^*(t_k), U_3^*(t_k)\} + 2U_0^*(t_k) = 0 \tag{4.22}$$

Further, (4.22) will transformed into (4.23):

$$U_0^*(t_k) = -\frac{1}{2}[max\{U_1^*(t_k), U_2^*(t_k), U_3^*(t_k)\} + min\{U_1^*(t_k), U_2^*(t_k), U_3^*(t_k)\}] \tag{4.23}$$

In (4.23), zero sequence average voltage value $U_0^*(t_k)$ has been completely defined in every sample period. According to this definition, pulse centering unit proposed in [21] is introduced to a three-output/three-input structure which is shown in Figure 4.6:

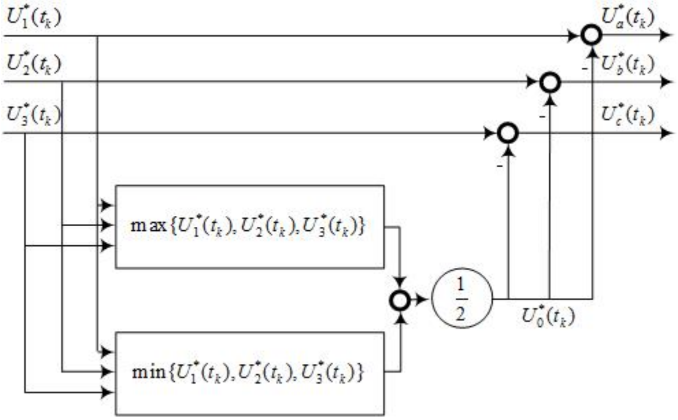

Figure 4.6: Three-Phase Pulse Centering Module [21]

Similarly, Figure 4.7 describes the space vector modulation in Simulink.

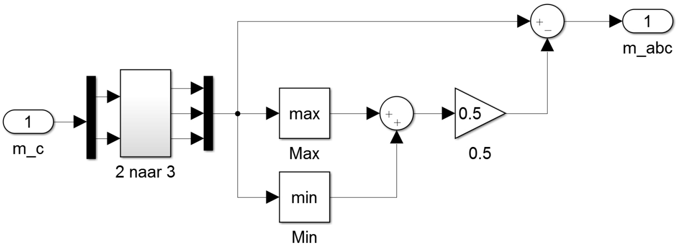

Figure 4.7: Space Vector Modulation

4.3. POWER ELECTRONIC CONVERTER

IN power electronic converter, there are two back to back converters between the grid and CW called grid side converter [22] and machine side converter and the grid side converter controls the dc-link voltage, which is a rectifier to convert the input AC voltage into DC voltage and the machine side converter controls the current in CW. In this thesis, the machine side converter is paid more attention and it is assumed that when low voltage dip condition occurs, due to the large capacitance of the capacitor, dc-link voltage will keep stable. In addition, considering the back to back converter is a partially rated converter, the speed range will be kept from 70 % to 130 % of the natural speed which corresponds Figure 2.8. Figure 4.8 indicates the structure of power electronic converter in Simulink and it can be seen that the important technology in it is the SPWM.

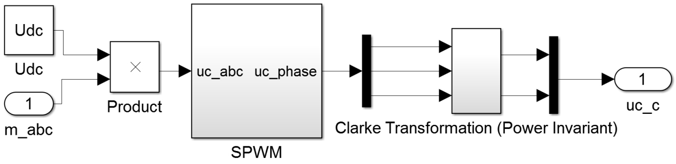

Figure 4.8: Power Electronic Converter

4.3.1. SINUSOIDAL PULSE WIDTH MODULATION

In Sinusoidal Pulse Width Modulation (SPWM), the output of the three-phase pulse centering module is the modulation signal and $\frac{1}{2}U_{dc}$ multiplies the triangle wave is the carrier signal. Figure 4.9 displays the SPWM based on the three-phase pulse centering module:

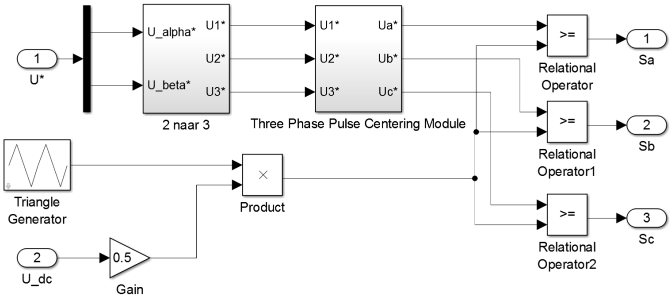

Figure 4.9: SPWM Based on Three-Phase Pulse Centering Module

After the SPWM, switch signals can be achieved. For the values of S_a, S_b and S_c, there are only two situations in each switch: 0 and 1. One means the IGBT is closed and zero represents it opens, which is the gate signal of switches (IGBT) in three-phase converter.

4.3.2. THREE-PHASE CONVERTER

A three-phase converter converts the dc-link voltage into three-phase SPWM waveforms based on the gate signal of switches. Figure 4.10 shows the bidirectional three-phase converter in Simulink based on the switch signals from Figure 4.9. The output of this converter is the CW voltage u_c.

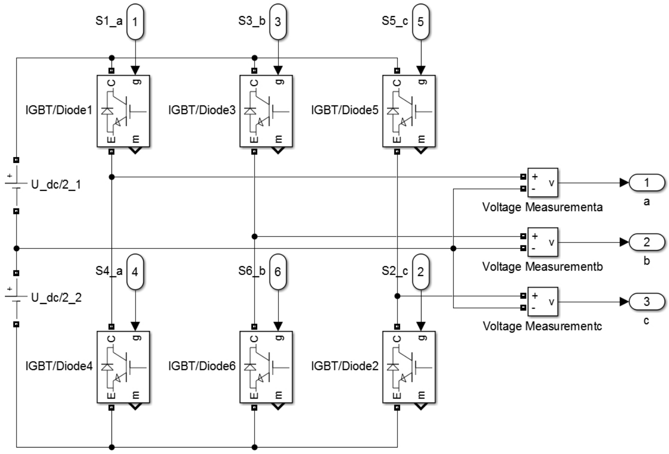

Figure 4.10: Three-Phase Converter

4.4. CONTROL STRATEGY PERFORMANCE SIMULATION

HAVING built the complete model of B-DFIG, simulations should be implemented to verify the feasibility of the controller. In the controller, there are two control loops: current loop and speed loop. First, PI tuning should be done. When tuning current loop, speed loop is omitted first and the inertia of the rotor shaft is set infinite to keep speed always being zero. A small step reference signal is used to check the reference current value and real current value. When the real current value can follow the reference current value, the current controller tuning is finished. Then the inertia of the rotor shaft should be recovered and the same method is applied to tuning the speed controller. After these two controllers are ready, the controller tuning is finished. Figure 4.11 and 4.12 give controller behaviours when speeds are 420 rpm (sub-synchronous mode) and 780 rpm (super-synchronous mode). In these figures, arbitrary small d-axis CW current i_{cd} and small load torque T_l have been given as 2 A and 2 Nm respectively to prove the rationality of the speed controller and current controller. To avoid saturation, 100 V is given at the terminal of PW arbitrarily. The parameters of B-DFIG are based on Table 2.1.

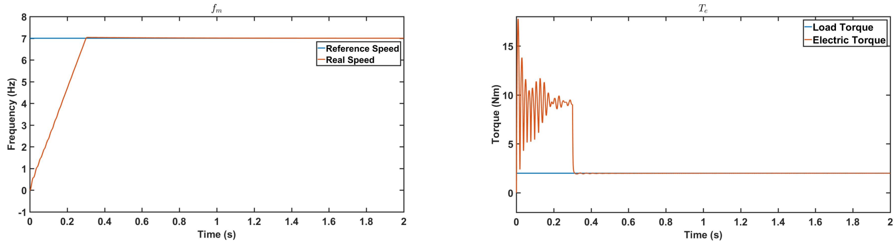

(a) Mechanical Frequency

(b) Torque

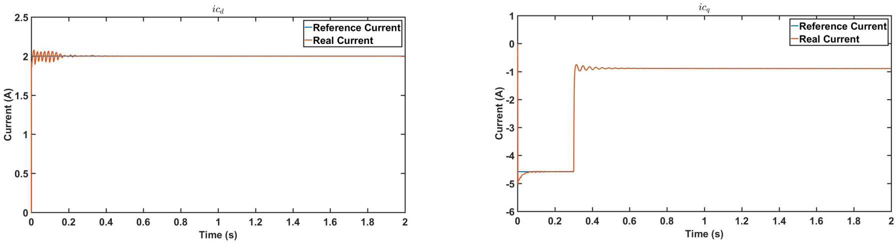

(c) d-axis CW Current

(d) q-axis CW Current

Figure 4.11: Controller Behaviour at Sub-synchronous Mode (420 rpm)

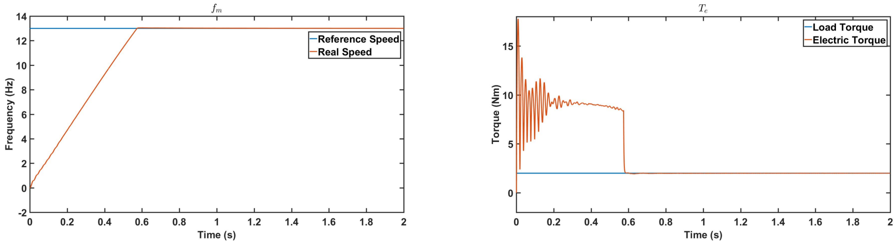

(a) Mechanical Frequency

(b) Torque

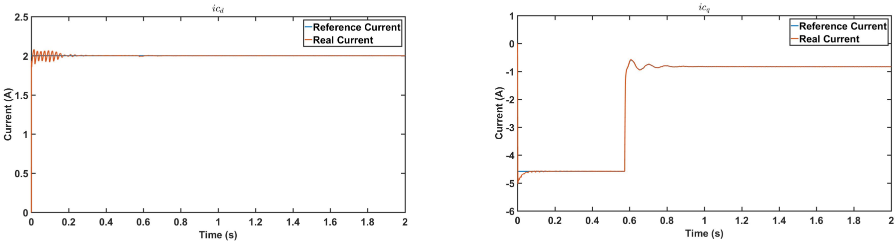

(c) d-axis CW Current

(d) q-axis CW Current

Figure 4.12: Controller Behaviour at Super-synchronous Mode (780 rpm)

From these figures, it can be seen that at start, when the real speed increases from zero to reference speed, B-DFIG provides a large i_{cq} to supply an electric torque which should be larger than the load torque. In that case, the machine has an acceleration to speed up. Due to the same acceleration while unequal speed differences, the transient time is also different in two modes (about 0.3 s and 0.6 s respectively). When the real speed is equal to the reference speed, i_{cq} reduces to the steady state value to generate lower electric torque as same as the load torque. Basically, the real speed can follow the speed reference signal by speed controller and the electric torque is equal to load torque in steady state. In addition, dq-axis CW current can also follow the reference values in steady state. Therefore, the PI controllers are reasonable for this B-DFIG model in this speed range.

Current Response

To demonstrate the performance of the d-axis current control loop, the dynamic behaviour of a d-axis CW current step response is simulated. At time 1 s, i_{cd} decreases from 2 A to 50 % (1 A), Figure 4.13 indicates the machine's response:

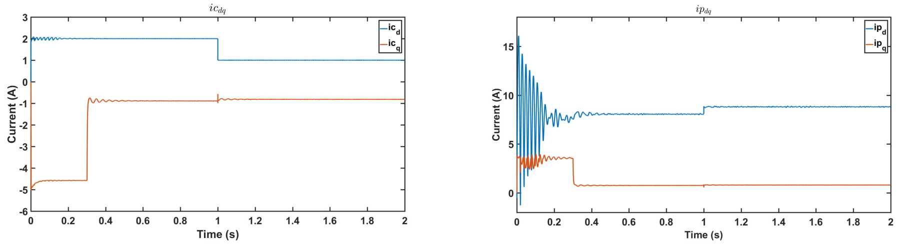

(a) dq-axis CW Current (b) dq-axis PW Current

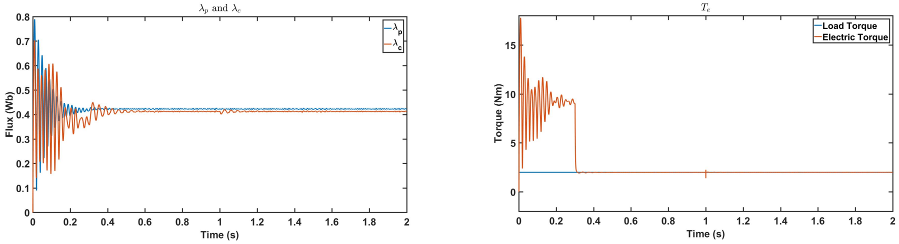

(c) PW and CW Flux (d) Torque

Figure 4.13: Result of Step Response of d-axis CW Current

In Figure 4.13, it can be seen that when i_{cd} decreases from 100 % to 50 % of original value, i_{pd} starts to go up to keep the flux being constant. Similarly, when i_{cd} tends to rise, i_{pd} will ramp down to avoid the increase of total flux. In addition, q-axis current does not change in this whole process, hence the electric torque always keeps stable.

Speed Response

To give the performance of q-axis speed control loop, the dynamic behaviour of speed step response is simulated. At the same time, if the reference speed decreases from super-synchronous speed to sub-synchronous speed (from 13 Hz to 7 Hz), the machine's response is described in Figure 4.14.

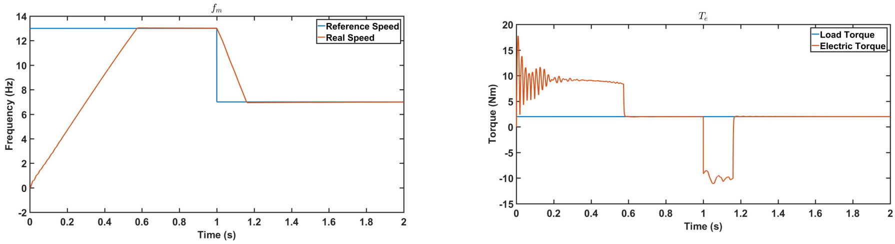

(a) Mechanical Frequency (b) Torque

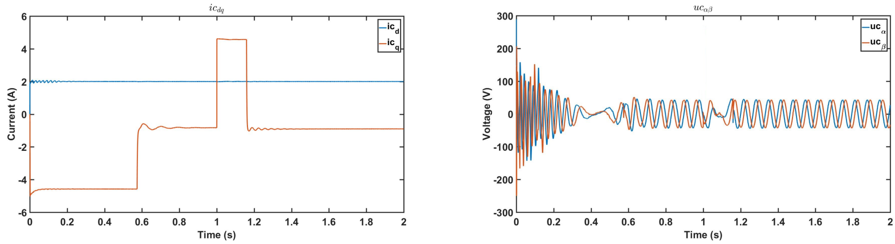

(c) dq-axis CW Current (d) $\alpha\beta$-axis CW Voltage

Figure 4.14: Result of Step Response of Speed

In Figure 4.14, it can be observed that at 1 s, f_m reference signal decreases from 13 Hz to 7 Hz. Due to the differential equation of mechanical frequency, the real f_m cannot change suddenly. To slow down the speed, T_e will decrease. T_e reduces to negative value directly to provide an enough deceleration for slowing down the speed. To achieve this requirement, the value of i_{cq} changes from negative to positive value. In the figure of $u_{\alpha\beta}$ (Figure 4.14 (d)), the sequences of α component and β component are changed at around 1.1 s, because B-DFIG runs from super-synchronous mode into sub-synchronous mode. Similarly, when f_m reference signal increases from 7 Hz to 13 Hz at 1 s, the principle will be the same as speed decrease situation. The only difference is that the direction of change is opposite to before.

Torque Response

To show the performance of q-axis current control loop, the dynamic behaviour of torque step response is simulated. At $t = 1s$, load torque T_l decreases from 4 Nm to 2 Nm. The behaviour of B-DFIG is described in Figure 4.15:

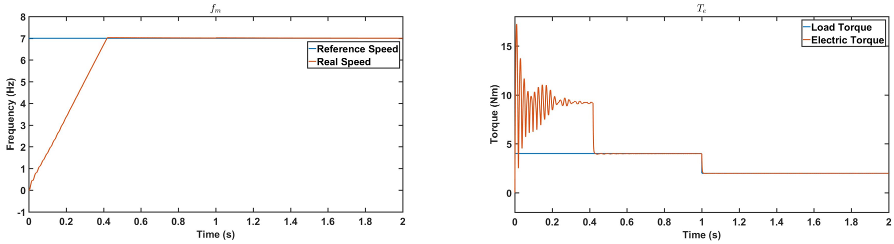

(a) Mechanical Frequency

(b) Torque

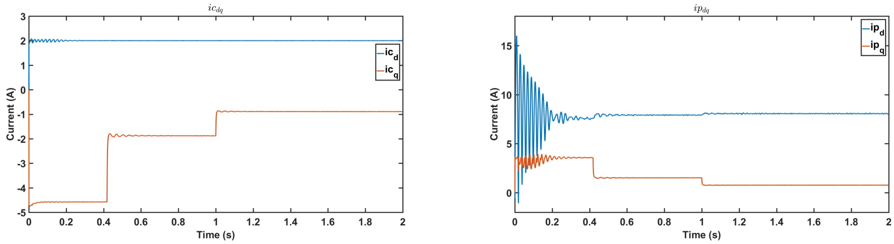

(c) dq-axis CW Current

(d) dq-axis PW Current

Figure 4.15: Result of Step Response of Load Torque

In Figure 4.15, at $t = 1s$, T_l decreases from 100 % to 50 % of original value. However, to keep the speed being constant, i_{cq} reduces immediately to produce lower electric torque. In this control strategy, the dq-axis components have been decoupled completely, which means that the flux only depends on d-axis current and the torque only depends on q-axis current. In that case, when the load torque changes, i_{cd} and i_{pd} will keep stable, hence the flux in both PW and CW also will maintain the previous values. The step response of d-axis CW current in Figure 4.13 also corresponds to this situation (In Figure 4.13, the situation is that the change of i_{cd} does not affect i_{cq}). According to (4.8), when T_e becomes 50 % of original value, i_{cq} reduces from -1.8 A to -0.9 A. Similarly, due to the relationship between i_{pq} and i_{cq}, i_{pq} also halves. In addition, when the load torque increases from 2 Nm to 4 Nm at 1 s, the changing direction of variables will be opposite to the previous trend.

The reference signals of these three step response simulations are based on the values in controller behaviour simulations which are shown in Figure 4.11 and 4.12. Small values have been given arbitrarily to test the feasibility of the control strategy.

4.5. SUMMARY

THE control strategy called Sensorless FOC has been described in this chatper. In this control strategy, the actual rotor shaft position does not need to be known while the flux position angle is used instead. For the main part of the controller, it has two control loops: current loop and speed loop respectively. However, the control strategy has divided the current vector into d-axis and q-axis and two axes have been decoupled. In that case, one axis controls one kind of variable. The reactive power (flux) only depends on d-axis value and the active power (torque) is only related to q-axis component. After two control loops, the space vector modulation is built. Through three-phase pulse centering module and the SPWM, the CW voltage signal can be achieved from the three-phase power electronic converter.

Having built the complete B-DFIG model, some simulations are implemented on this model. These simulations are based on different aspects, speed range simulations, current step response, speed step response and load torque step response. From these simulations, control manners can be known clearly from this model and the B-DFIG can operate at synchronous mode successfully using this control strategy, which proves the feasibility of the controller. It is very useful to the simulation in both full voltage and low voltage dip conditions in Chapter 5.

REFERENCES

[1] R. Li, R. Spee, A. K. Wallace, and G. Alexander, *Synchronous drive performance of brushless doubly-fed motors,* IEEE Transactions on Industry Applications **30**, 963 (1994).

[2] D. Zhou, R. Spee, and A. Wallace, *Laboratory control implementations for doubly-fed machines,* in *Industrial Electronics, Control, and Instrumentation, 1993. Proceedings of the IECON'93., International Conference on* (IEEE, 1993) pp. 1181–1186.

[3] S. Shao, E. Abdi, and R. McMahon, *Operation of brushless doubly-fed machine for drive applications,* (2008).

[4] P. Zhang, G. Y. Sizov, M. Li, D. M. Ionel, N. A. Demerdash, S. J. Stretz, and A. W. Yeadon, *Multi-objective tradeoffs in the design optimization of a brushless permanent-magnet machine with fractional-slot concentrated windings,* IEEE Transactions on Industry Applications **50**, 3285 (2014).

[5] R. Zhao, A. Zhang, Y. Ma, X. Wang, J. Yan, and Z. Ma, *The dynamic control of reactive power for the brushless doubly fed induction machine with indirect stator-quantities control scheme,* IEEE Transactions on Power Electronics **30**, 5046 (2015).

[6] A. Zhang, X. Wang, W. Jia, and Y. Ma, *Indirect stator-quantities control for the brushless doubly fed induction machine,* IEEE Transactions on Power Electronics **29**, 1392 (2014).

[7] F. Barati, R. McMahon, S. Shao, E. Abdi, and H. Oraee, *Generalized vector control for brushless doubly fed machines with nested-loop rotor,* IEEE transactions on industrial electronics **60**, 2477 (2013).

[8] A. Broekhof, R. McMahon, and J. Maciejowski, *Decoupling method for vector control of the brushless doubly-fed machine,* in *Industrial Electronics Society, IECON 2013-39th Annual Conference of the IEEE* (IEEE, 2013) pp. 3457–3462.

[9] Z. S. Du and T. A. Lipo, *Dynamics and vector control of wound-rotor brushless doubly fed induction machines,* in *Energy Conversion Congress and Exposition (ECCE), 2014 IEEE* (IEEE, 2014) pp. 1332–1339.

[10] S. Ademi and M. G. Jovanović, *Vector control methods for brushless doubly fed reluctance machines,* IEEE Transactions on Industrial Electronics **62**, 96 (2015).

[11] R. Cardenas, R. Peña, S. Alepuz, and G. Asher, *Overview of control systems for the operation of dfigs in wind energy applications,* IEEE Transactions on Industrial Electronics **60**, 2776 (2013).

[12] G. D. Marques and M. F. Iacchetti, *Stator frequency regulation in a field-oriented controlled dfig connected to a dc link,* IEEE Transactions on Industrial Electronics **61**, 5930 (2014).

[13] D. D. Reigosa, F. Briz, C. Blanco, and J. M. Guerrero, *Sensorless control of doubly fed induction generators based on stator high-frequency signal injection,* IEEE Transactions on Industry Applications **50**, 3382 (2014).

[14] S. Yang and V. Ajjarapu, *A speed-adaptive reduced-order observer for sensorless vector control of doubly fed induction generator-based variable-speed wind turbines,* IEEE Transactions on energy conversion **25**, 891 (2010).

[15] L. Xu, E. Inoa, Y. Liu, and B. Guan, *A new high-frequency injection method for sensorless control of doubly fed induction machines,* IEEE Transactions on Industry Applications **48**, 1556 (2012).

[16] S. Shao, E. Abdi, F. Barati, and R. McMahon, *Stator-flux-oriented vector control for brushless doubly fed induction generator,* IEEE Transactions on Industrial Electronics **56**, 4220 (2009).

[17] J. Poza, E. Oyarbide, I. Sarasola, and M. Rodriguez, *Vector control design and experimental evaluation for the brushless doubly fed machine,* IET Electric Power Applications **3**, 247 (2009).

[18] S. Shao, T. Long, E. Abdi, and R. A. McMahon, *Dynamic control of the brushless doubly fed induction generator under unbalanced operation,* IEEE Transactions on Industrial Electronics **60**, 2465 (2013).

[19] T. Long, S. Shao, P. Malliband, E. Abdi, and R. A. McMahon, *Crowbarless fault ride-through of the brushless doubly fed induction generator in a wind turbine under symmetrical voltage dips,* IEEE Transactions on Industrial Electronics **60**, 2833 (2013).

[20] T. Strous, *Brushless doubly fed induction machines for wind turbine drive-train applications,* (2016).

[21] R. De Doncker, D. W. Pulle, and A. Veltman, *Advanced electrical drives: analysis, modeling, control* (Springer Science & Business Media, 2010).

[22] P. S. Flannery and G. Venkataramanan, *Unbalanced voltage sag ride-through of a doubly fed induction generator wind turbine with series grid-side converter,* IEEE Transactions on Industry Applications **45**, 1879 (2009).

5

B-DFIG LVRT SIMULATION

5.1. INTRODUCTION

HAVING built the complete B-DFIG model and testified the feasibility of the controller, B-DFIG behaviours simulation under full voltage and low voltage dip conditions should be implemented. Firstly, LVRT is defined and explained. Secondly, simulations under both full voltage and low voltage dip conditions are done in the model with control strategy and B-DFIG performance will be compared between full voltage and low voltage dip conditions. The results of simulation also will be compared with the outcomes of experiments in Chapter 7.

5.2. LOW VOLTAGE RIDE THROUGH

THE definition of LVRT is the capability of generators to stay connected to the grid in short periods of low voltage dip [1]. In a generator, current flowing through windings produce the magnetic field. To keep a certain value of magnetic field, there is a minimum working voltage in the terminal of excited windings, below which the machine does not work normally or works at reduced efficiency. Traditionally, the machine will be disconnected the from the grid when low voltage dip condition occurs. This phenomenon is more obvious in DFIG which have two sets of windings and lower leakage inductance. In squirrel-cage induction generators, there is only one winding, hence the effect is not very pronounced. Synchronous generators may slip and become unstable, if the voltage of the stator winding goes below a certain threshold. In B-DFIG, due to the larger leakage inductance in rotor part than DFIG, the influence of low voltage dip is less serious than DFIG, while it still needs to be improved in low voltage dip condition. In wind turbine, the machine needs to be connected to the grid when a certain low voltage dip occurs in a short period of time, which means that it ’rides through’ low voltage. When the low voltage dip level exceeds the minimum voltage level or the faulty time is longer than the maximum time, the machine should be disconnected from the grid in low voltage dip and when voltage level recovers, the machine will be connected back to the grid.

5.3. BEHAVIOUR IN FULL VOLTAGE CONDITION

IN Chapter 4, dynamic behaviours of B-DFIG have been simulated by different kinds and different groups of simulations and the control strategy runs successfully for this machine. Therefore, the simulation should start from the full voltage condition to observe in normal operations, what the B-DFIG behaviours are. LVRT always occurs at the generator mode of B-DFIG. The convention of this machine's model is that when the load torque is positive, machine is in motor mode and the power flows into the machine (the value of power is positive). When the load torque is negative, machine is in generator mode and the power is negative (flows out of B-DFIG). Firstly, reasonable assumptions are proposed based on [2] as follows:

1. In LVRT mode, the speed of the machine is considered being constant, but in reality, machine's speed tends to increase during the low voltage dip, because the power generating into the grid has been reduced in low voltage dip and the extra power will become kinetic energy in the rotor part. However, due to the short period of faulty time and large inertia of the rotor shaft, the speed increase is generally small. Therefore, constant speed of B-DFIG in low voltage dip condition is widely used in B-DFIG LVRT analysis.

2. The proposed LVRT control strategy in this thesis is only exerted on machine side converter and the grid side converter is not studied. The grid side converter in B-DFIG is the same as that in DFIG, which has been proposed in [3][4]. The B-DFIG in the lab does not have a grid side converter while only uses a constant dc-link voltage instead. To make the situation between simulation and experiment as similar as possible, it is assumed that during the low voltage dip, dc-link voltage does not change [5] due to the large capacitor in parallel with it while in reality, it will be a bit fluctuations.

3. In this thesis, only symmetrical voltage dips are considered, because in the whole B-DFIG model, the zero sequence components of variables are assumed to be zero and then they can be omitted. However, in asymmetrical voltage dips, the zero sequence components of variables are not zero, hence they cannot be ignored.

When assumptions have been proposed, it should be known what the reference values will be given in this model. There are two reference signals i_{cd} and f_m. f_m reference signal is the expected mechanical frequency of B-DFIG and in this model, the speed will vary from 70 % to 130 % of natural speed, which is from 7 Hz to 13 Hz. The limitation of the equipment in experiment are dc-link voltage and current which are 200 V and 5 A. If losses are ignored, the relationship between the input and the output of the inverter is shown in (5.1):

$$U_{dc}I_{dc} = 3u_{ac}i_{ac} \tag{5.1}$$

U_{dc} is the dc-link voltage and u_{ac} means CW phase voltage which is PWM waveform. The amplitude of this PWM waveform is $\pm\frac{1}{2}U_{dc}$. In linear modulation [6], the maximum amplitude of the output of the inverter (fundamental field) is $\frac{1}{2}U_{dc}$, so the relationship between U_{dc} and rms value of u_{ac} is displayed in (5.2):

$$U_{dc} \geq 2\sqrt{2}u_{ac} \tag{5.2}$$

Therefore, the relationship between I_{dc} and i_{ac} is shown in (5.3):

$$i_{ac} \geq \frac{2\sqrt{2}}{3} I_{dc} \tag{5.3}$$

According to (5.3), when $I_{dc} = 5A$, $i_{ac} = 4.71A$ and if $i_{ac} \leq 4.71A$ (the amplitude of $i_{ac} \leq 6.67A$), both the voltage and current will not exceed the limitation of the equipment in experiment, which is the safety region, so the constraint of this thesis is to keep the CW phase current below 4.71 A all the time. Under full voltage condition, the CW and PW phase current in sub-synchronous and super-synchronous speed in generator mode is given in Figure 5.1. The PW phase voltage is kept same as that in Chapter 4.4 (100 V). The parameters of B-DFIG is in Table 2.1.

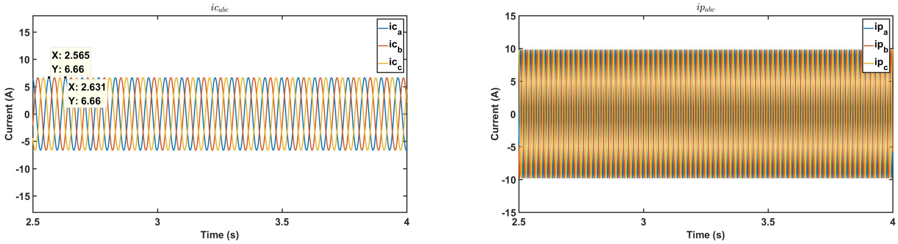

(a) CW Phase Current (420 rpm)

(b) PW Phase Current (420 rpm)

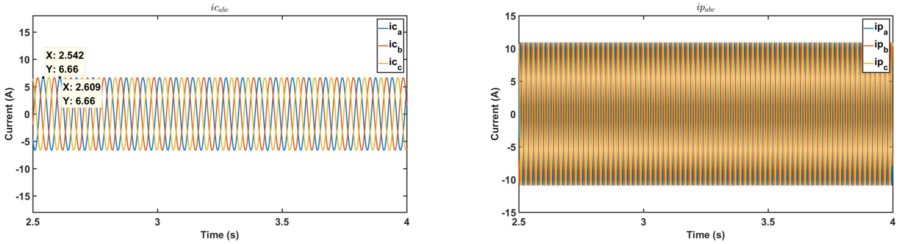

(c) CW Phase Current (780 rpm)

(d) PW Phase Current (780 rpm)

Figure 5.1: Sub-synchronous and Super-synchronous Behaviours under full voltage Condition ((a) and (b) in sub-synchronous speed, (c) and (d) in super-synchronous speed)

In Figure 5.1, some conclusions can be got as follows:

1. The period and frequency of CW phase current is 0.067 s and 15 Hz respectively in both modes, which corresponds to the (2.13). f_{ce} depends on the mechanical frequency when the frequency of grid and pole pairs of both PW and CW are fixed.

2. In sub-synchronous mode, the sequence of CW current is a-b-c while in super-synchronous mode, the sequence becomes a-c-b.

3. In both modes, the steady state CW phase current amplitude is around 6.67 A, which is the largest current case. Under full voltage and low voltage dip conditions, the

largest current case is simulated, which means the load torque reaches the maximum load torque. Therefore, in lower load torque condition, it is easier to make B-DFIG ride through low voltage.

Having achieved the steady state value of CW phase current in full voltage condition, simulations are implemented in low voltage condition.

5.4. BEHAVIOUR IN LOW VOLTAGE DIP CONDITION

To imitate the low voltage dip in reality, 3 different low voltage dip levels are given in this section: 25 %, 50 % and 75 % of voltage dips respectively. Figure 5.2 describes different kinds of voltage dip levels in PW. Figure 5.3 and 5.4 indicate the current and flux in PW and CW and the mechanical frequency under 25 %, 50 % and 75 % of low voltage dips in sub-synchronous and super-synchronous modes respectively. The fault time is from 3 s to 3.5 s and the constant speed can be realized by setting a large inertia in low voltage dip condition.

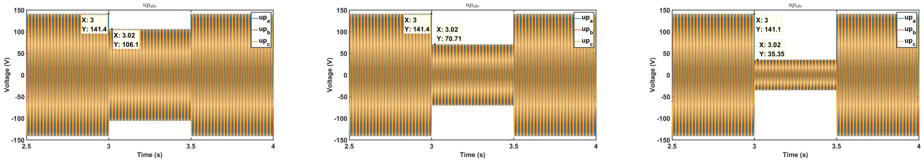

(a) 25 % of Voltage Dip (b) 50 % of Voltage Dip (c) 75 % of Voltage Dip

Figure 5.2: Different kinds of PW Phase Voltage Dips

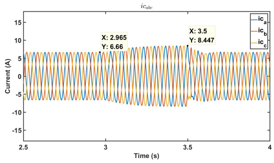

(a) CW Phase Current (b) CW Phase Current (c) CW Phase Current

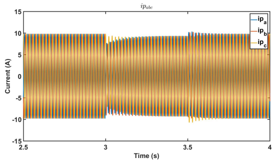

(d) PW Phase Current (e) PW Phase Current (f) PW Phase Current

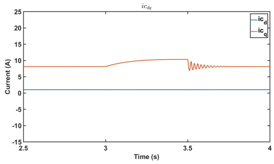

(g) dq-axis CW Current (h) dq-axis CW Current (i) dq-axis CW Current

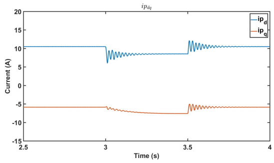

(j) dq-axis PW Current (k) dq-axis PW Current (l) dq-axis PW Current

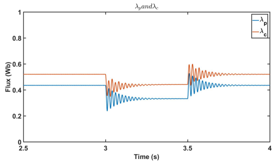

(m) Flux in PW and CW (n) Flux in PW and CW (o) Flux in PW and CW

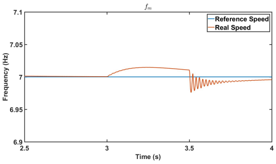

(p) Mechanical Frequency (q) Mechanical Frequency (r) Mechanical Frequency

Figure 5.3: Sub-synchronous Behaviour (420 rpm) with Constant Speed under Low Voltage Dip Condition ((a), (d), (g), (j), (m) and (p) in 25 % of voltage dip, (b), (e), (h), (k), (n) and (q) in 50 % of voltage dip, (c), (f), (i), (l), (o) and (r) in 75 % of voltage dip)

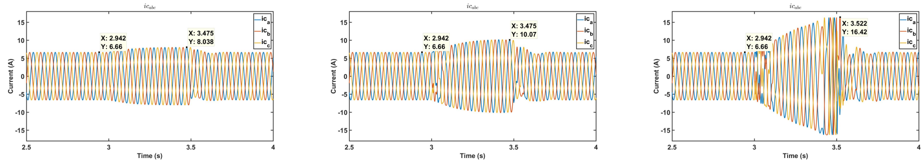

(a) CW Phase Current (b) CW Phase Current (c) CW Phase Current

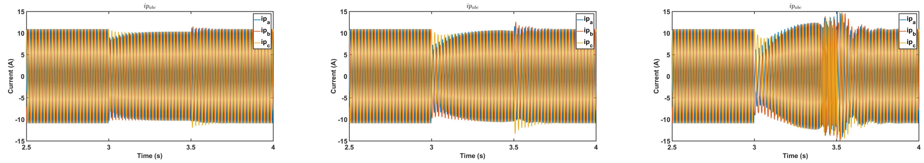

(d) PW Phase Current (e) PW Phase Current (f) PW Phase Current

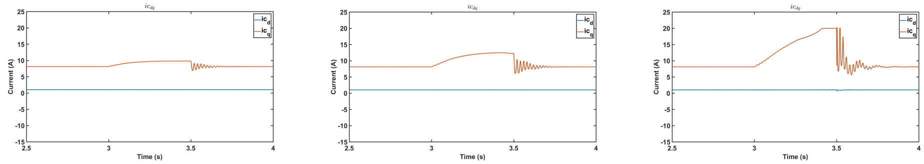

(g) dq-axis CW Current (h) dq-axis CW Current (i) dq-axis CW Current

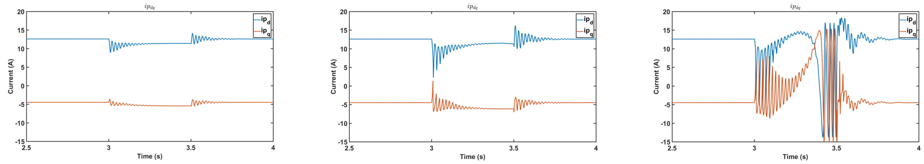

(j) dq-axis PW Current (k) dq-axis PW Current (l) dq-axis PW Current

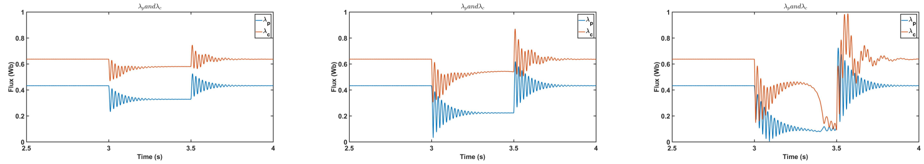

(m) Flux in PW and CW (n) Flux in PW and CW (o) Flux in PW and CW

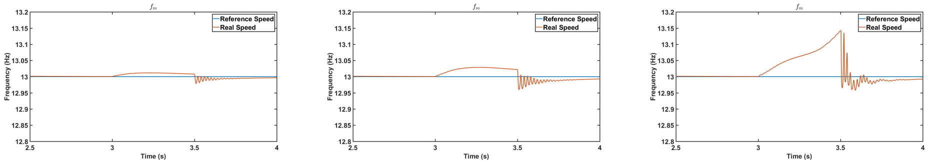

(p) Mechancial Frequency (q) Mechanical Frequency (r) Mechanical Frequency

Figure 5.4: Super-synchronous Behaviour (780 rpm) with Constant Speed under Low voltage Dip Condition ((a), (d), (g), (j), (m) and (p) in 25 % of voltage dip, (b), (e), (h), (k), (n) and (q) in 50 % of voltage dip, (c), (f), (i), (l), (o) and (r) in 75 % of voltage dip)

In these figures, when low voltage dip occurs, the CW phase current will start to increase, because the flux decreases with the PW phase voltage dip, which has been validated through differential equations and shown in Figure 'Flux in PW and CW'. According to (4.8), the electric torque depends on the flux and q-axis CW current. To make sure the electric torque can carry the load torque, higher q-axis CW current is necessary to produce the previous value of the electric torque. When d-axis CW current does not change due to the constant d-axis CW reference current, there is a large transient CW current. In addition, when low voltage dip condition occurs, the CW phase current increment depends on the voltage dip level. The larger voltage dip is, the higher current increment is. Obviously, 75 % of voltage dip is more serious than other two cases. At this situation, CW phase current becomes more than twice as large as steady state CW phase current (4.71 A).

However, in real wind turbine, when low voltage dip occurs, the speed of rotor cannot be kept constant. B-DFIG only can deliver less power to the grid due to the low voltage dip while the speed of wind does not change, so the extra energy becomes kinetic energy into the rotor part. In that case, the rotor starts to speed up. Figure 5.5 and 5.6 describe the current and flux in PW and CW with non-constant speed under 25 %, 50 % and 75 % of low voltage dips in sub-synchronous and super-synchronous modes respectively.

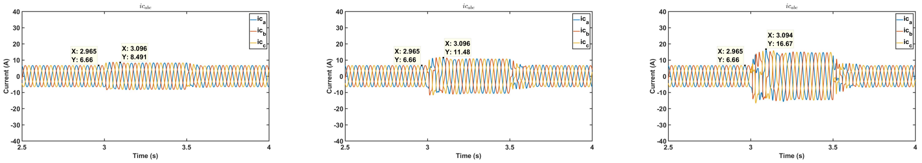

(a) CW Phase Current (b) CW Phase Current (c) CW Phase Current

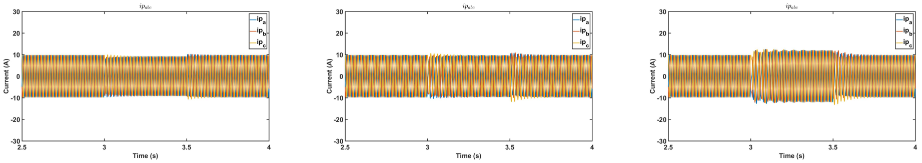

(d) PW Phase Current (e) PW Phase Current (f) PW Phase Current

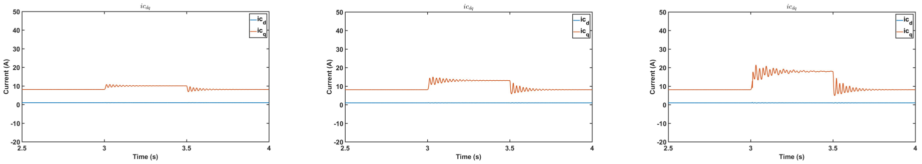

(g) dq-axis CW Current (h) dq-axis CW Current (i) dq-axis CW Current

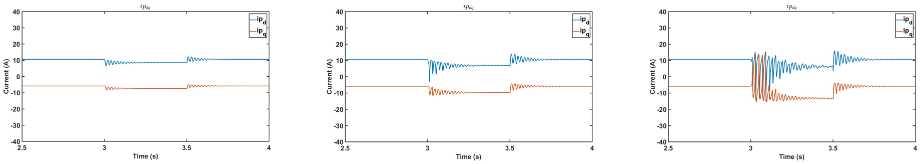

(j) dq-axis PW Current (k) dq-axis PW Current (l) dq-axis PW Current

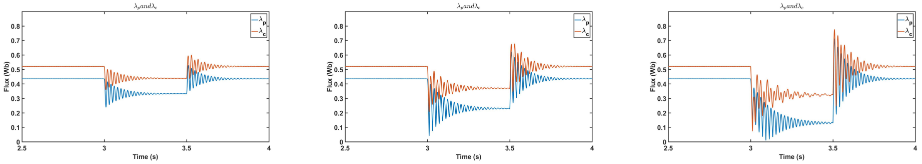

(m) Flux in PW and CW (n) Flux in PW and CW (o) Flux in PW and CW

Figure 5.5: Sub-synchronous Behaviour (steady state: 420 rpm) with Non-constant Speed under Low Voltage Dip Condition ((a), (d), (g), (j) and (m) in 25 % of voltage dip, (b), (e), (h), (k) and (n) in 50 % of voltage dip, (c), (f), (i), (l) and (o) in 75 % of voltage dip)

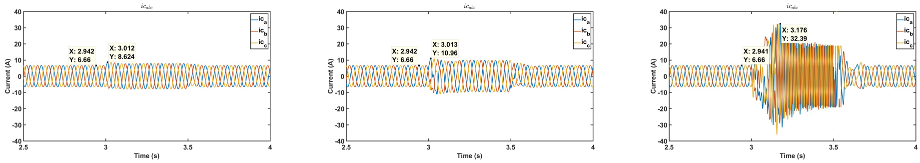

(a) CW Phase Current (b) CW Phase Current (c) CW Phase Current

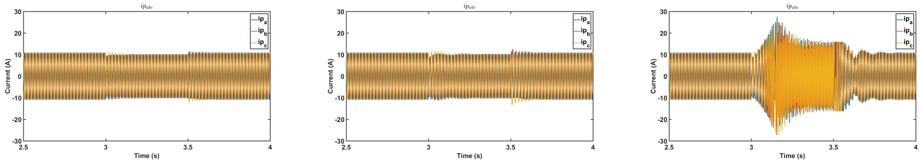

(d) PW Phase Current (e) PW Phase Current (f) PW Phase Current

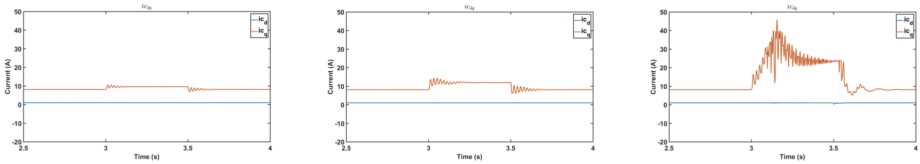

(g) dq-axis CW Current (h) dq-axis CW Current (i) dq-axis CW Current

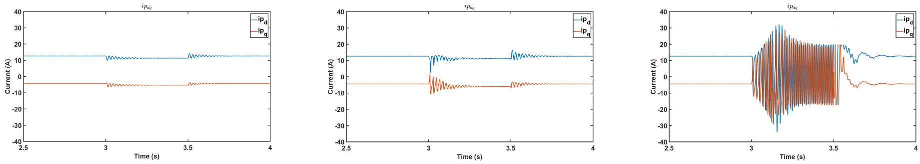

(j) dq-axis PW Current (k) dq-axis PW Current (l) dq-axis PW Current

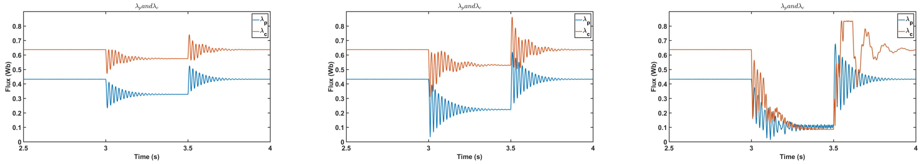

(m) Flux in PW and CW (n) Flux in PW and CW (o) Flux in PW and CW

Figure 5.6: Super-synchronous Behaviour (steady state: 780 rpm) with Non-constant Speed under Low voltage Dip Condition ((a), (d), (g), (j) and (m) in 25 % of voltage dip, (b), (e), (h), (k) and (n) in 50 % of voltage dip, (c), (f), (i), (l) and (o) in 75 % of voltage dip)

From these figures, it can be seen that the transient current in CW is larger than that with constant speed, because the increment of speed generates larger power and this power stays at the PW and CW. In addition, non-constant speed takes a large transient current immediately in CW while in constant speed situation, the transient current in CW increases gradually instead, which also because the extra kinetic energy becomes electric power into CW. Moreover, to make the simulation environment as similar as that in experiment, the dc-link voltage keeps stable all the time. However, in reality, if CW delivers power to the grid, dc-link voltage will increase and if CW absorbs power from the grid, dc-link voltage will decrease. Therefore the grid side converter also should be considered while in this thesis, it is ignored. In addition, symmetrical voltage dip (three-phase voltage dip) does not often occur in industry while asymmetrical voltage dip such as single-phase voltage dip and phase to phase voltage dip always happen. Therefore, these three assumptions have their own limitations due to the constraints of the equipment in experiment.

5.5. SUMMARY

BFORE simulation, reasonable assumptions are raised and maximum CW phase current is also given based on constraints of the equipment in experiment. Then simulations have been implemented under full voltage condition in both sub-synchronous and super-synchronous modes. After these simulations, the steady state value of CW phase current is achieved as the reference in low voltage dip simulation. In low voltage dip condition, machine's behaviours have been simulated in different low voltage dip levels in both sub-synchronous and super-synchronous modes. Unexpected performance of B-DFIG can be concluded in low voltage dip condition. The problem appears that the transient current in CW is too large, which is harmful to the power electronic converter. This unexpected larger CW transient current will be limited in Chapter 6.

REFERENCES

[1] Wikipedia, *Low voltage ride through — wikipedia, the free encyclopedia,* (2017), [Online; accessed 18-September-2017].

[2] S. Shao, T. Long, E. Abdi, R. McMahon, and Y. Wu, *Symmetrical low voltage ride-through of the brushless doubly-fed induction generator,* in *IECON 2011-37th Annual Conference on IEEE Industrial Electronics Society* (IEEE, 2011) pp. 3209–3214.

[3] O. Gomis-Bellmunt, A. Junyent-Ferre, A. Sumper, and J. Bergas-Jane, *Ride-through control of a doubly fed induction generator under unbalanced voltage sags,* IEEE Transactions on Energy Conversion **23**, 1036 (2008).

[4] Y. Zhou, P. Bauer, J. A. Ferreira, and J. Pierik, *Operation of grid-connected dfig under unbalanced grid voltage condition,* IEEE Transactions on Energy Conversion **24**, 240 (2009).

[5] D. Xiang, L. Ran, P. J. Tavner, and S. Yang, *Control of a doubly fed induction generator in a wind turbine during grid fault ride-through,* IEEE Transactions on Energy Conversion **21**, 652 (2006).

[6] N. Mohan and T. M. Undeland, *Power electronics: converters, applications, and design* (John Wiley & Sons, 2007).

6

B-DFIG LVRT CONTROL ALGORITHM

6.1. INTRODUCTION

HAVING simulated B-DFIG behaviours in different conditions, it is found that the transient CW current is so large that destroy the power electronic converter. Through analyzing the cause of this unexpected performance of the machine, solutions can be discovered to improve B-DFIG behaviours. Therefore, the LVRT control algorithm (injecting reactive current) is proposed step by step to make sure the machine can ride through low voltage naturally, which is the most meaningful part in this thesis.

6.2. LVRT CONTROL ALGORITHM

IN section 5.4, the large transient CW current produced under low voltage dip condition will be harmful to the power electronic converter. Therefore, in this section, it should be known which factor will influence the transient CW current more and how to limit transient CW current in an acceptable value. Larger voltage dip level affects the CW current more and in this thesis, there are three voltage dip levels: 25 %, 50% and 75 %. Obviously, 75 % of voltage dip is more severe than other two cases in LVRT, hence it should be studied first. Having solved the problem in this situation, this LVRT control algorithm can also be applied in other voltage dip levels. Due to the constraints of the equipment in experiment, CW phase current is limited under 4.71 A to protect the power electronic converter. The maximum CW phase current produces a largest electric torque which is equal to the load torque. This load torque is the maximum load torque that the machine can carry. The influence of different load torque levels is described in Figure 6.1 under 75 % of voltage dip condition (75 %, 50 %, 25 % and 0 % of maximum load torque respectively).

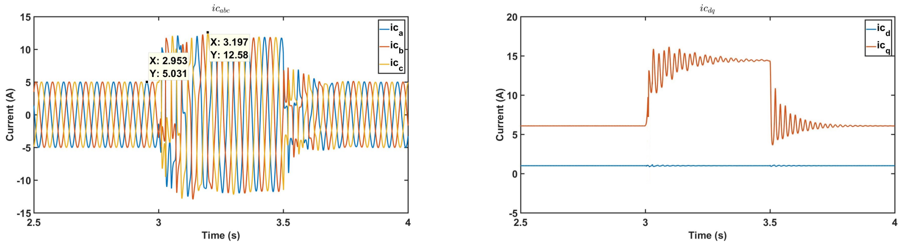

(a) CW Phase Current under 75 % of Maximum Load Torque

(b) dq-axis CW Current under 75 % of Maximum Load Torque

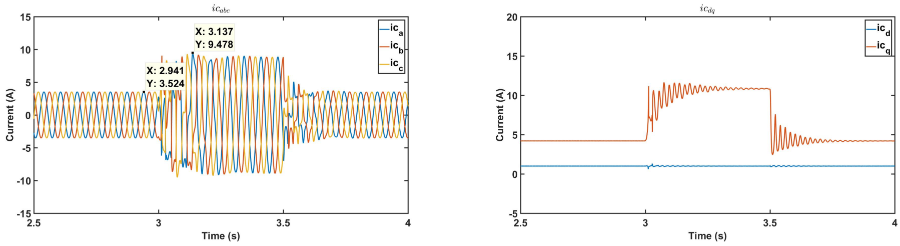

(c) CW Phase Current under 50 % of Maximum Load Torque

(d) dq-axis CW Current under 50 % of Maximum Load Torque

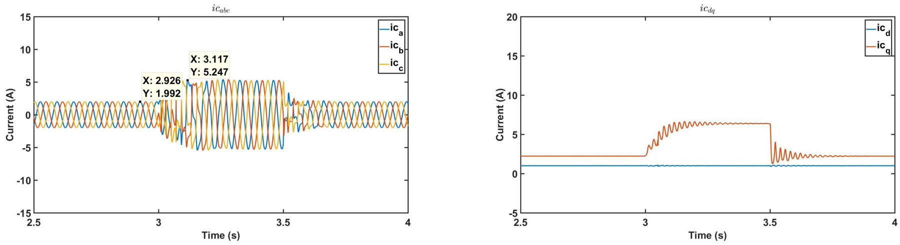

(e) CW Phase Current under 25 % of Maximum Load Torque

(f) dq-axis CW Current under 25 % of Maximum Load Torque

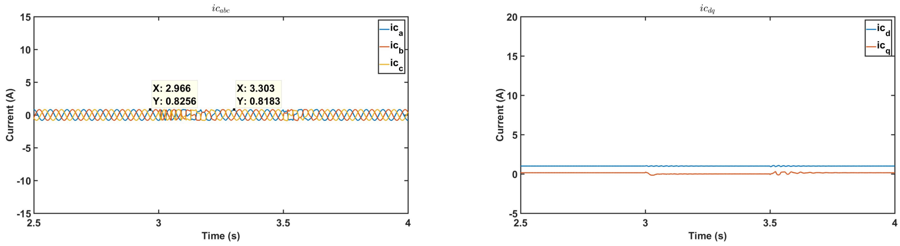

(g) CW Phase Current under 0 % of Maximum Load Torque

(h) dq-axis CW Current under 0 % of Maximum Load Torque

Figure 6.1: CW Current under 75 % of Voltage Dip in different Load Torque Levels

In Figure 6.1, conclusions are discovered as follows:

1. Larger load torque will take larger steady state CW phase current.

2. When low voltage dip occurs, larger load torque will lead to larger transient CW phase current.

3. In 25 % of the maximum load torque condition, even though in 75 % of voltage dip, CW phase current still does not exceed 4.71 A. In other words, the machine has ridden through low voltage naturally. Therefore, when the load torque is less than 25 % of the maximum load torque, it is not necessary to do any operations in low voltage dip condition.

4. For no load simulation, CW phase current will not increase in low voltage dip any more, because when low voltage dip occurs, due to the decrease of flux in both PW and CW and according to (4.8), generating larger q-axis CW current is the only way to realize keeping electric torque following with the load torque. However, when the load torque is zero, q-axis CW current will be always zero before and after low voltage dip condition. Therefore, CW phase current will not increase any more in the low voltage dip condition.

When low voltage dip occurs, PW voltage decreases a lot, so B-DFIG deliver less active power to the grid. However, the speed of wind does not change and the extra large amount of active power will generate a large current in CW, which is harmful to the power electronic converter. Reactive current can be injected at this time to support PW voltage. In that case, the transient CW current will reduce effectively in a reasonable level.

For LVRT, the main objective is limiting the CW phase current below the maximum value to protect the power electronic converter. When low voltage dip occurs, the grid can only absorb less active power, hence it is wise to inject reactive current to support the grid voltage. Therefore, the proposed LVRT control algorithm [1] is concluded step by step as follows:

1. When detecting rms value of PW phase voltage is lower than a threshold voltage, the low voltage dip situation is measured and the controller starts to shift into LVRT mode. Hysteresis comparison is applied in this thesis to eliminate faulty detection.

2. In LVRT mode, the speed controller is not required and the control algorithm starts to inject reactive current into the grid. Before LVRT mode, the steady state value of i_c was recorded in dq-axis reference frame. After LVRT is detected, i_{cd} reference signal is set the steady state value of $|i_c|$ and i_{cq} is given zero.

3. When rms value of PW phase voltage is higher than the threshold voltage, it means the grid fault has been cleared. The speed loop can be connected back and i_{cd} reference signal will be given the pre-fault value again. The controller turns back to the normal control strategy.

The proposed LVRT control algorithm is shown in Figure 6.2:

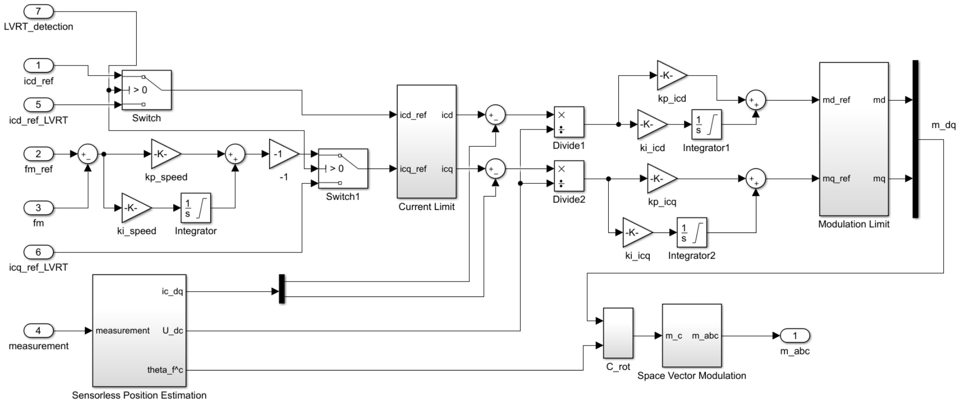

Figure 6.2: LVRT Control Algorithm

In this figure, when PW phase voltage is higher than the threshold value, LVRT detection will give a positive output and the switches turn on the normal control strategy. However, when PW phase voltage is lower than the threshold value, LVRT detection gives a negative output and switches shift to the LVRT control mode. The steady state dq-axis CW current ($i_{cd} = |i_c^{dq}|$ and $i_{cq} = 0$) will be given into the input of current limit.

6.3. RESULTS AND ANALYSIS

USING the proposed control algorithm in section 6.2, B-DFIG behaviours are described in Figure 6.3 and 6.4 under different low voltage dip levels in both sub-synchronous and super-synchronous modes.

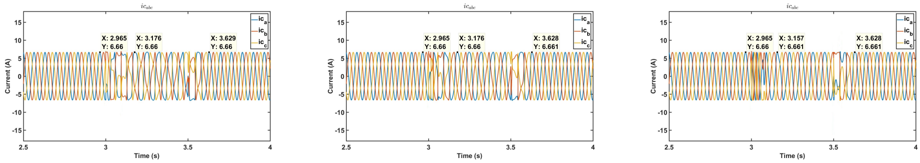

(a) CW Phase Current (b) CW Phase Current (c) CW Phase Current

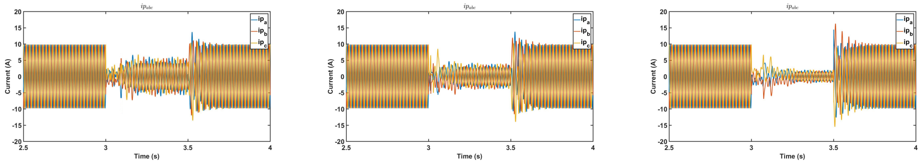

(d) PW Phase Current (e) PW Phase Current (f) PW Phase Current

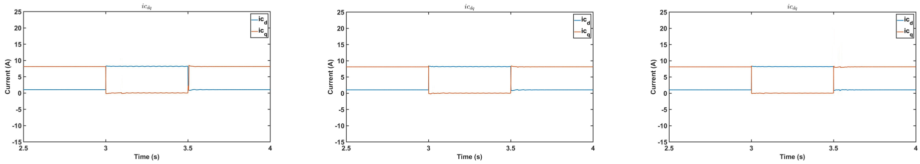

(g) dq-axis CW Current (h) dq-axis CW Current (i) dq-axis CW Current

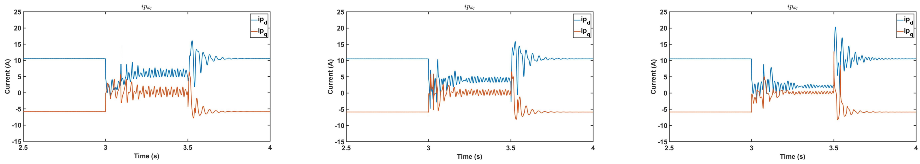

(j) dq-axis PW Current (k) dq-axis PW Current (l) dq-axis PW Current

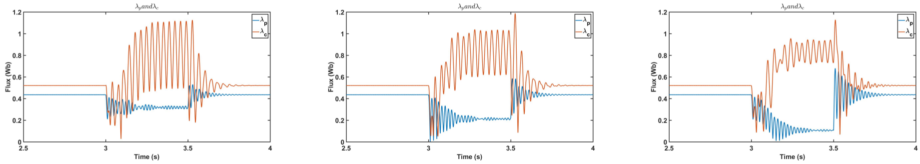

(m) Flux in PW and CW (n) Flux in PW and CW (o) Flux in PW and CW

Figure 6.3: Sub-synchronous Behaviour (420 rpm) under Low Voltage Dip Condition with LVRT Control Algorithm ((a), (d), (g), (j) and (m) in 25 % of voltage dip, (b), (e), (h), (k) and (n) in 50 % of voltage dip, (c), (f), (i), (l) and (o) in 75 % of voltage dip)

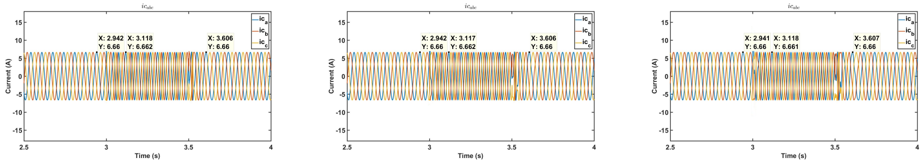

(a) CW Phase Current (b) CW Phase Current (c) CW Phase Current

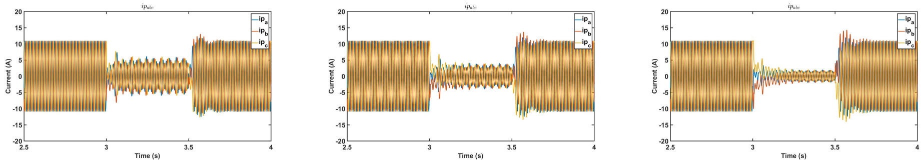

(d) PW Phase Current (e) PW Phase Current (f) PW Phase Current

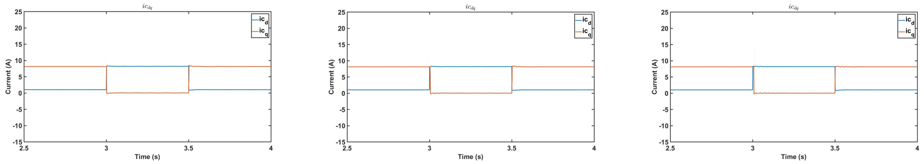

(g) dq-axis CW Current (h) dq-axis CW Current (i) dq-axis CW Current

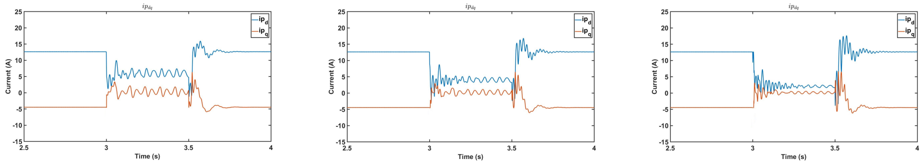

(j) dq-axis PW Current (k) dq-axis PW Current (l) dq-axis PW Current

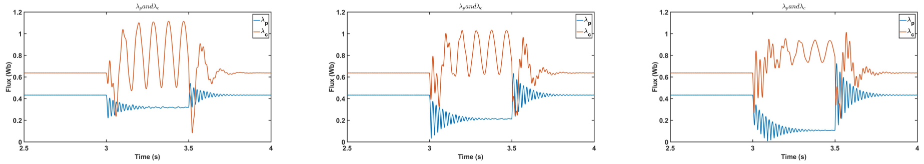

(m) Flux in PW and CW (n) Flux in PW and CW (o) Flux in PW and CW

Figure 6.4: Super-synchronous Behaviour (780 rpm) under Low Voltage Dip Condition with LVRT Control Algorithm ((a), (d), (g), (j) and (m) in 25 % of voltage dip, (b), (e), (h), (k) and (n) in 50 % of voltage dip, (c), (f), (i), (l) and (o) in 75 % of voltage dip)

From these figures, it can be observed that before low voltage dip, the current in both PW and CW reached at the steady state values. When low voltage dip condition occurs, reactive current is injected into the grid to support CW flux, so the CW transient current has been reduced under the maximum value. However, when fault is cleared, due to the transient voltage increment in PW, the flux in PW will increase immediately. After the flux in PW and CW recover the previous value, the machine has ridden through low voltage totally and the controller turns to the normal control strategy. In addition, all of these simulations are implemented in the largest load torque condition which is the worst situation. Therefore, when the load torque becomes lower, the machine can still ride through low voltage completely by the proposed LVRT control algorithm. Until now, the LVRT control algorithm is reasonable for this machine's model in LVRT mode.

However, in simulation, all of conditions are so ideal that the LVRT control algorithm is perfect. It can control the CW phase current in LVRT mode as same as that in normal mode, which cannot be realized in reality. In addition, these three assumptions are also unrealistic in industry. The speed tends to increase in LVRT mode, dc-link voltage will have a bit fluctuation and the three-phase voltage dip cannot be symmetrical totally. Therefore, CW phase current in LVRT mode will not be equal to the value of that in normal mode.

6.4. SUMMARY

WHEN simulations under full voltage and low voltage dip conditions have been implemented, the problems will be found that the transient CW current is so large that destroy the power electronic converter. Reactive current should be injected in this low voltage dip condition to support the PW voltage. Having chosen the worst condition: 75 % of voltage dip and maximum load torque, proposed constraints and reasonable assumptions, the LVRT control algorithm is shown step by step in this chapter. Finally, through the proposed LVRT control algorithm, B-DFIG has ridden through low voltage successfully, which gives meaningful guidances and directions for the LVRT experiment in Chapter 7.

REFERENCES

[1] S. Shao, T. Long, E. Abdi, R. McMahon, and Y. Wu, *Symmetrical low voltage ride-through of the brushless doubly-fed induction generator,* in *IECON 2011-37th Annual Conference on IEEE Industrial Electronics Society* (IEEE, 2011) pp. 3209–3214.

7

B-DFIG LVRT EXPERIMENT

7.1. INTRODUCTION

To compare the B-DFIG behaviours between simulation and experiment, experiments are going to be implemented on B-DFIG, which consists of parameters measurement, low voltage dip producing, behaviours under full voltage and low voltage dip conditions. In parameters measurement, parameters such as resistance and inductance are measured based on equivalent circuits to give references in simulation. In low voltage dip producing, a voltage divider circuit is used, which contains two inductors and contactors. Contactors always work in high voltage environment and the switching time of them is very short, hence another control circuit is designed to switch contactors. For the contactor control circuit, the microcontroller is programmed to control the power relays close or open and then contactors can be switched by power relays. By changing the ratio between two inductors, this voltage divider can produce different low voltage dip levels at the terminal of B-DFIG to imitate the low voltage dip condition in reality. Finally, B-DFIG behaviours are measured in experiment and are simulated to make a comparison under full voltage and low voltage dip conditions.

7.2. PARAMETERS MEASUREMENT

To make sure the consistency of parameters of B-DFIG in simulation and experiment, parameter measurements are done to verify that. Table 7.1 and 7.2 give the original measurement results in the experiment.

u_p (V)	R_p (Ω)	i_p (A)	f_p (Hz)	p_p	n_s (rpm)	n (rpm)
100	0.77	3.79	50	3	1000	1000

Table 7.1: Measurement Results in PW

u_c (V)	R_c (Ω)	i_c (A)	f_c (Hz)	p_c	n_s (rpm)	n (rpm)
100	0.7	2.53	50	2	1500	1500

Table 7.2: Measurement Results in CW

Parameters measurements are done based on the equivalent circuit proposed in [1] of B-DFIG which is shown in Figure 2.2. In both PW and CW experiments, a winding is connected to the grid and the other one is open circuit, which is in simple mode of operation. The equivalent circuits have been described in Figure 2.4 and in these experiments, the speed of rotor has been set as the synchronous speed to make sure the slip of the machine is zero. Therefore, the equivalent circuits in Figure 2.4 are transformed into Figure 7.1:

(a) CW Open Circuit (b) PW Open Circuit

Figure 7.1: Equivalent Circuit of B-DFIG in Simple Mode

In Figure 7.1, according to the data in Table 7.1 and 7.2, inductance can be calculated in Table 7.3:

L_p (H)	L_σ (H)	L_c (H)
0.084	0.023	0.1027

Table 7.3: Inductance of B-DFIG

In Figure 2.2, all of the leakage inductance has been converted into CW. Therefore, in Figure 7.1 (b), the CW inductance contains two parts: main inductance and leakage inductance. Based on parameters measurement in [2], through some comparisons between simulation and experiment, the ratio can be estimated between L_c and L_σ. In addition, the turn ratio between PW and CW: $n_{pw} : n_{cw}$ and resistance of rotor can also be estimated. All of the parameters of B-DFIG are shown in Table 2.1.

7.3. Low Voltage Dip Producing

Different low voltage dip levels are going to be built at the terminal of the machine in this section. In reality, when large loads are connected to the grid or as a result of grid faults like lightning strikes or short circuits, short–term voltage dip may occur [3]. This low voltage dip condition is planned to be simulated at the terminal of PW. After that, under this situation, some experiments will be implemented to test and analyze the behaviours of B-DFIG.

7.3.1. VOLTAGE DIVIDER

For the low voltage establishment, there is a voltage divider proposed in [3] shown in the Figure 7.2:

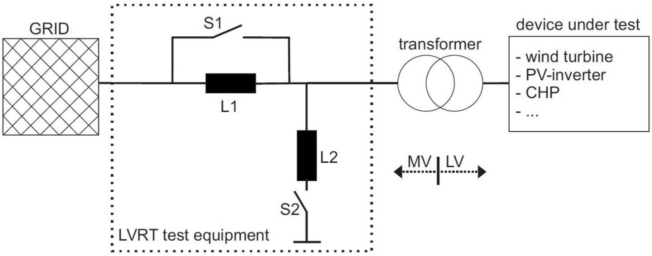

Figure 7.2: Voltage Divider [3]

This voltage divider contains two contactors: L1 and L2 in one phase, which can have several coils in both series and parallel connection. When S1 is close and S2 is open, the terminal voltage is equal to the grid voltage while when S1 is open and S2 is close, the terminal voltage is equal to $\frac{L2}{L1+L2}$ multiplies the grid voltage. Different voltage levels can be achieved by changing the ratio between L1 to L2. Contactors are working in high voltage environment and the switch time of them is just several milliseconds and switching. Therefore, the contactor control circuits are designed to solve this problem.

7.3.2. CONTACTOR CONTROL CIRCUIT

The contactor control circuit is displayed in Figure 7.3:

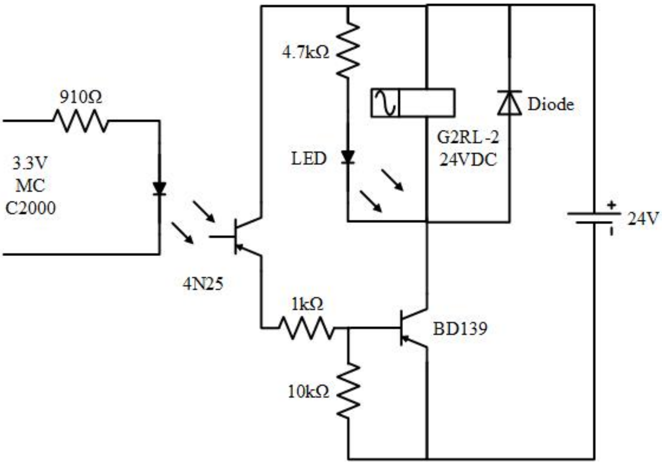

Figure 7.3: Contactor Control Circuit

This circuit is connected to a contactor. By programming the microcontroller, it controls the power relay to switch the contactor closed or opened. Through this method, required voltage dip levels can be produced at the terminal of the power supply. There are some main components in the contactor control circuit such as optocoupler and power relay.

OPTOCOUPLER

The physical picture and schematic of optocoupler (4N25) are indicated in Figure 7.4:

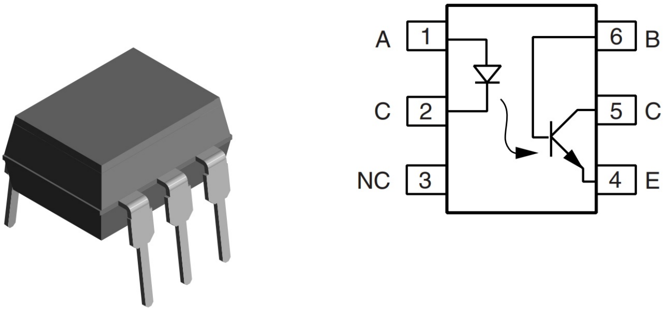

Figure 7.4: Optocoupler (4N25) [4]

Optocoupler is a component which transfers electrical signals between two isolated circuit by using light. An optocoupler prevents high voltage from affecting the system receiving the signal. It contains a source (emitter) of light, almost always a near infrared light-emitting diode (LED) which converts electrical input signal into light, a closed optical channel (also called dielectrical channel) and a photosensor that detects incoming light and either generates electrical energy directly or modulates current flowing from an external power supply [5].

POWER RELAY

The physical picture and internal circuit of the power relay (G2RL-2 24VDC) is shown in Figure 7.5:

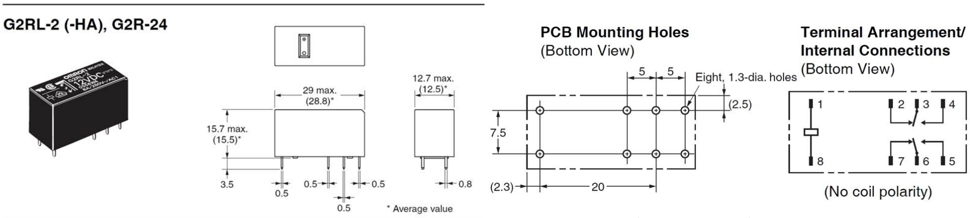

(a) Power Relay (G2RL-2 24VDC)

(b) Internal Circuit

Figure 7.5: Physical Picture and Internal Circuit of the Power Relay [6]

Power relay is an electrically operated switch, which use an electromagnet to mechanically operate a switch. Relays are used where it is necessary to control a circuit by a separate low-power signal, or where several circuits must be controlled by one signal [7].

CONTACTOR

The physical picture and rated voltage for the contactor (ESB 20-11) is displayed in Figure 7.6:

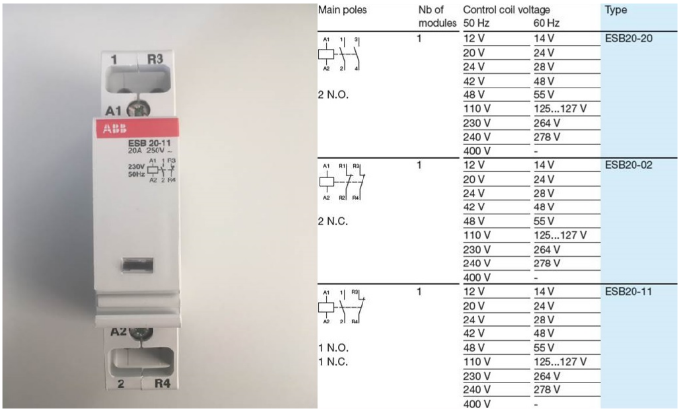

Main poles	Nb of modules	Control coil voltage 50 Hz	60 Hz	Type
2 N.O.	1	12 V	14 V	ESB20-20
		20 V	24 V	
		24 V	28 V	
		42 V	48 V	
		48 V	55 V	
		110 V	125...127 V	
		230 V	264 V	
		240 V	278 V	
		400 V	-	
2 N.C.	1	12 V	14 V	ESB20-02
		20 V	24 V	
		24 V	28 V	
		42 V	48 V	
		48 V	55 V	
		110 V	125...127 V	
		230 V	264 V	
		240 V	278 V	
		400 V	-	
1 N.O. 1 N.C.	1	12 V	14 V	ESB20-11
		20 V	24 V	
		24 V	28 V	
		42 V	48 V	
		48 V	55 V	
		110 V	125...127 V	
		230 V	264 V	
		240 V	278 V	
		400 V	-	

Figure 7.6: Contactor [8]

A contactor is an electrically controlled switch which is always used for switching an electrical power circuit, similar to a power relay except with higher current ratings. A contactor is switched by a circuit that has a much lower power level than the switched circuit [9]. Operating principle of the contactor is that when the current passes through the electromagnet, magnetic field is produced, which attracts the moving core of the contactor. The moving contact is propelled by the moving core; the force produced by the electromagnet holds the moving and fixed contacts together. When the contactor coil is de-energized, gravity or a spring returns the electromagnet core to its initial position and open the contacts.

7.3.3. MICROCONTROLLER

At the left part of Figure 7.3, a microcontroller is connected to the circuit. Microcontroller is a small computer on a single integrated circuit. In modern society, it is a system on a chip or SOC. A microcontroller contains one or more CPUs along with memory and programmable input/output peripherals. Program memory in the form of Ferroelectric RAM, NOR flash or OTP. ROM is also often included on chip, as well as a small amount of RAM. Microcontroller is designed for embedded applications, in contrast to the microprocessors used in personal computers or other general purpose applications consisting of various discrete chips [10]. In this thesis, LAUNCHXL-F28027F is used, which is made by Texas Instrument (C2000). The function of the microcontroller is producing high or low voltage level to the left part of the optocoupler. Through the light, the signal will be converted into the right part of the optocoupler. In this condition, the power relay can be controlled closed or opened. Moreover, the contactor can be switched by the power relay and then the voltage divider can produce required voltage levels at the terminal of the power supply. The LAUNCHXL-F28027F is indicated in Figure 7.7, which is based on the microcontroller TMS320F28027F.

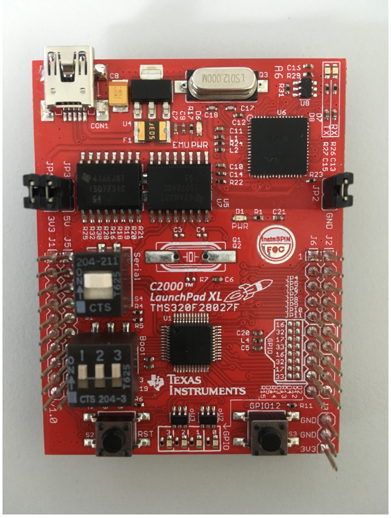

Figure 7.7: LAUNCHXL-F28027F

In Figure 7.3, when the microcontroller is connected to the left part of the contactor control circuit, it can control the power relay. If microcontroller gives a low voltage level (0 V) to the optocoupler, the transistor in optocoupler will not be turned on. There is no current flowing through the base of transistor BD139, hence it withstands the whole 24 V voltage. In that case, power relay does not work and LED is turned off. When the microcontroller gives a high voltage level (3.3 V) to the optocoupler, the LED in optocoupler will make the transistor in optocoupler turned on. The base current of transistor BD139 will also make itself turned on. The power relay works and LED starts to glow. This contactor control circuit is connected to the contactor. Through the status of power relays, contactors can also be switched. By this way, it realizes low voltage controls high voltage. In microcontroller, General Propose Input Output (GPIO) function is used to achieve this goal. Due to three-phase of PW and two contactors in one-phase voltage divider, there are 6 contactor control circuits in total. Therefore, 6 pins of GPIO are used to control the power relays and contactors. The schematic of LAUNCHXL-F28027F is given in Figure 7.8. In this figure and corresponding to the Figure 7.7, the location of GPIO0-GPIO5 pins can be found and then LAUNCHXL-F28027F is connected to 6 contactor control circuits. In addition, there are 4 LEDs which are connected to GPIO0-GPIO3. When GPIO0-GPIO3 are set to low voltage level, LEDs will be turned on and when GPIO0-GPIO3 are set to high voltage level, LEDs will be turned off. In that case, the voltage level of pins can be observed by observing LEDs. To produce low voltage dip, the switch S3 can be used, which is connected to GPIO12 and when pushing and holding the button S3, GPIO12 will be set high voltage level from low voltage level. Then GPIO0-GPIO5 will flip over and the status of 6 contactors can be changed. After a short period of time, GPIO0-GPIO5 will go back to previous states and 6 contactors flip again. In that case, low voltage dip can be produced. By changing the ratio between two inductor values, different low voltage dip levels can also be got at the terminal of the machine.

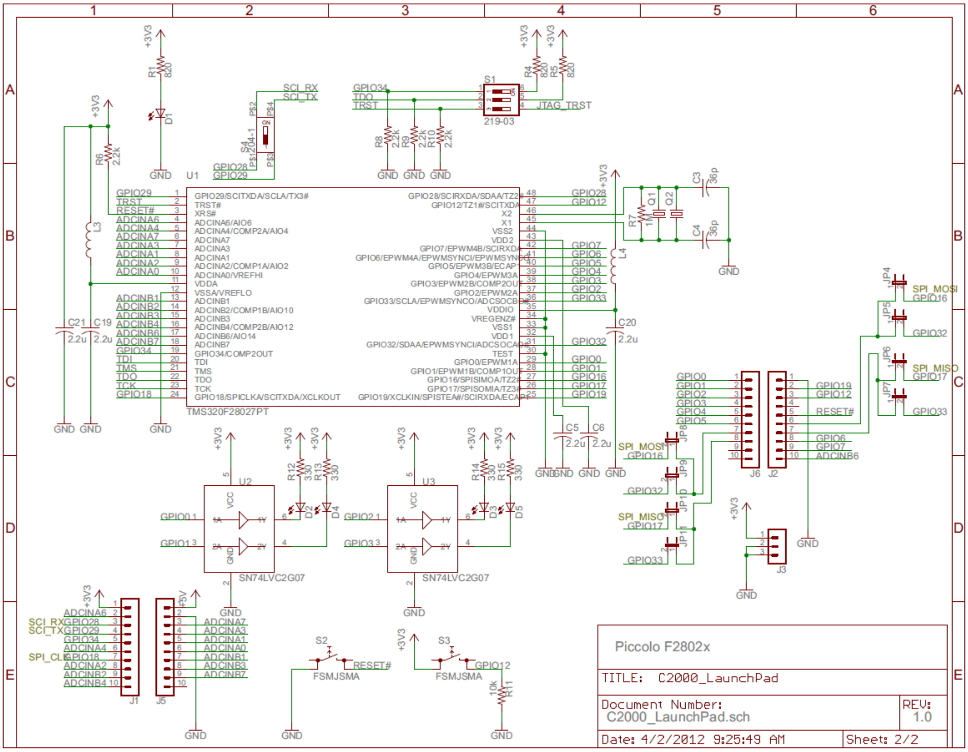

Figure 7.8: Schematic of LAUNCHXL-F28027F [11]

7.3.4. RESULT OF LOW VOLTAGE DIP

Having connected the microcontroller, contactor control circuits, contactors and inductors, different low voltage dip levels can be produced at the terminal of the power supply. Figure 7.9 describes the voltage divider in simulation and Figure 7.10 displays the simulation results by this voltage divider module.

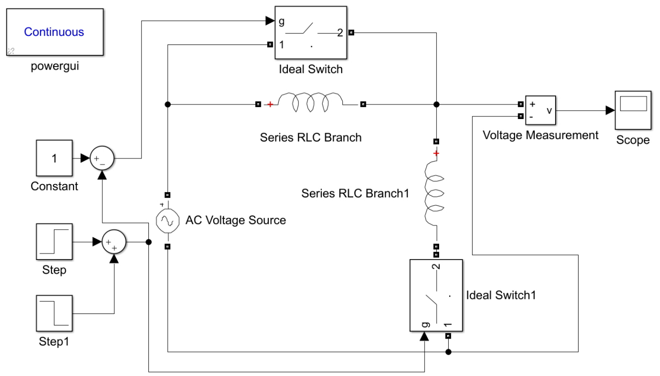

Figure 7.9: Voltage Divider Module

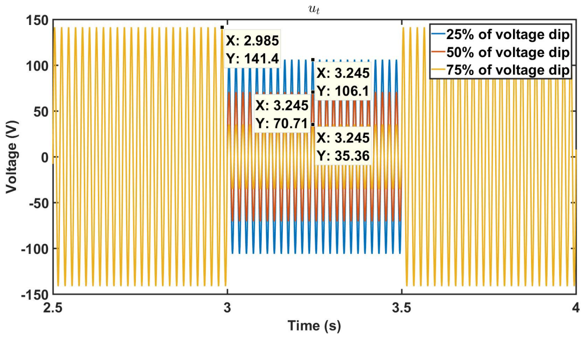

Figure 7.10: Terminal Voltage of B-DFIG in Simulation

Figure 7.11 shows the connection between microcontroller, contactor control circuits and contactors and Figure 7.12 displays inductors and the schematic of them. In Figure 7.12 (b), one circuit has 8 inductors and between two interfaces, there are two inductors. When connecting all of inductors in series, this circuit can produce 3 kinds of ratios between L1 and L2: 1:3, 1:1 and 3:1, which will make 25 %, 50 % and 75 % of voltage dip respectively.

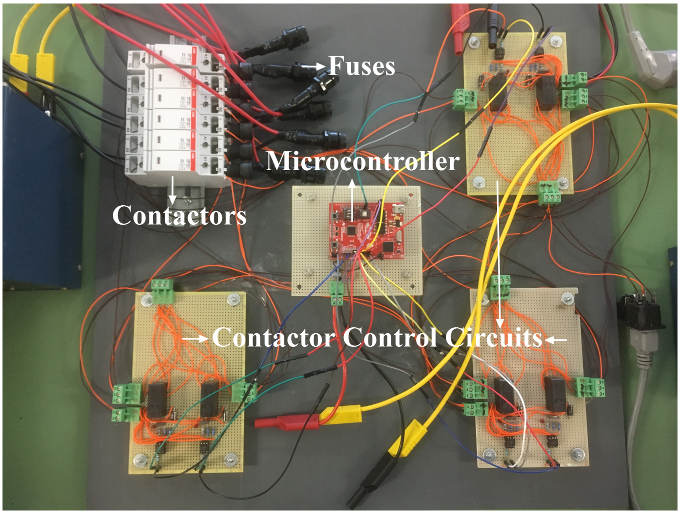

Figure 7.11: Contactor Control Circuit in Experiment

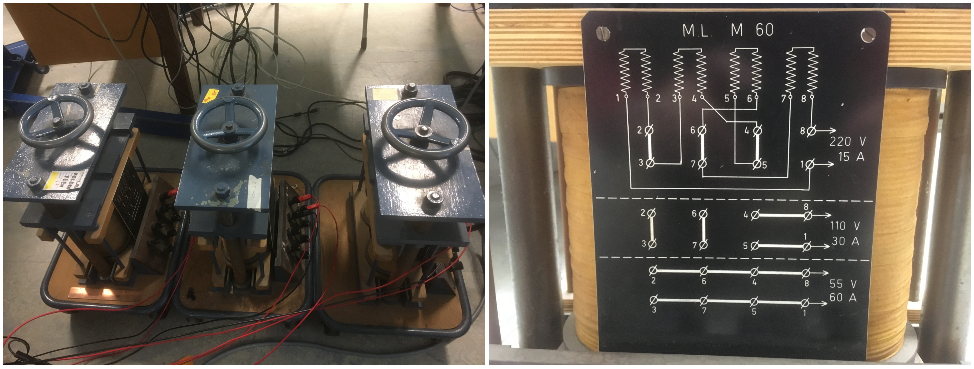

(a) Inductors (b) Schematic of Inductors

Figure 7.12: Inductors and Schematic of Inductors

Figure 7.13 describes the different voltage dip levels in phase A produced by voltage divider in experiment.

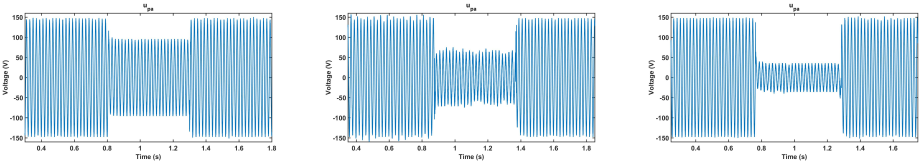

(a) 25 % of Voltage Dip (b) 50 % of Voltage Dip (c) 75 % of Voltage Dip

Figure 7.13: Different kinds of PW Phase Voltage Dips in Phase A

In these figures, it can be seen that the voltage dip time is about 0.5 s and the voltage dip levels correspond with that in simulation.

7.4. EXPERIMENT SETUP

THE experiment setup is presented to implement and describe a fully operational B-DFIG based drive, which is running through sensorless FOC strategy. Figure 7.14 indicates a schematic overview proposed in [1] of the experiment setup. This experiment setup consists of the following elements: a prototype B-DFIG, a partially power electronic converter, Power Supply Unit (PSU), mechanical load through a DC machine and a computer interface for programming the control strategy and controlling the drive.

7.4.1. THE PROTOTYPE B-DFIG

The B-DFIG used in the experiment setup is an early prototype machine, fitted in a D180 frame-size housing and developed by Delft University of Technology. Its specifications are given in Table 7.4 and Table 2.1. The PW of B-DFIG is connected to an iron-cored variable transformer to the 3-phase grid (50Hz). The CW of B-DFIG is connected to a partially power electronic converter. The rotor of B-DFIG is mechanically connected to an 11 kW DC machine which controlled by a commercial DC drive. Figure 7.14 (b) shows a picture of the B-DFIG connected to the DC machine.

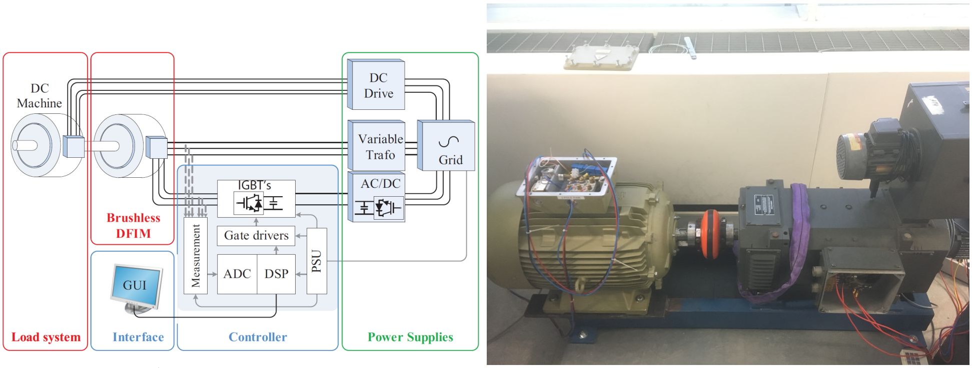

(a) Schematic Overview [2]

(b) B-DFIG (left) Connected to DC Machine (right)

Figure 7.14: B-DFIG Experiment Setup

Frame size		D180
Number of phases	N_{ph}	3
Number of stator slots	N_{ss}	72
Number of rotor slots	N_{rs}	40
Number of rotor nests	N_{nest}	5
Rotor loops per nest	q_r	4
PW		
Pole pairs	p_p	3
Turns per phase	N_p	144
CW		
Pole pairs	p_c	2
Turns per phase	N_c	120

Table 7.4: B-DFIG Design Parameters [2]

7.4.2. POWER ELECTRONIC CONVERTER AND CONTROL STRATEGY

For the implementation of the control strategy, a conventional full bridge inverter is shown, which is indicated in Figure 7.15. This inverter is stripped from an old industrial inverter unit excluding the heatsink, cooling fan, dc-link bus and a 15 V and 230 V PSU. This inverter is equipped with an another 5 V PSU, dc-link capacitors and 3 IGBT modules and their gate driver circuits. There are two IGBTs in a half-bridge configuration in each IGBT module (rated: 600 V, 300 A) and each IGBT has a reverse connected free-wheeling diode to absorb the reverse powerflow. The switching frequency of these modules is 16 kHz to control the voltage and frequency of CW. The PWM switching signal is calculated by the DSP and provided to the IGBT through their gate drivers. The dc-link voltage in the experimental setup is variable and is powered by a separate DC power supply.

Figure 7.15: Power Electronic Converter with DSP and the Electronic Circuit

The B-DFIG control strategy is implemented in the DSP. To realize this target, a Texas Instrument C2000 DSP experimenter kit is used (product code: TMSDOCK28069). This experimenter kit contains a docking station and a modular Piccolo F28069f control card (DSP), designed for control of electrical drives. It uses the flux, angle, seed, torque (FAST) integrated software function for encoderless flux and position estimation [12]. The FAST functions are used to determine the flux in both PW and CW, position angles, speed and torque. FAST measures the resistance of CW on the fly and it can measure the total leakage flux as seen from the CW during initialization, which is done by performing a blocked-rotor test with the PW being short circuit and then by forcing a high-frequency current flowing through the CW. This result in a high impedance path for the current through the main inductance, as can be seen from the equivalent circuit in Figure 3.1. The leakage inductance is then derived from the measured voltage and current. A deviation in leakage inductance will not produce a deviation in the steady state current and speed control values. Therefore, speed control is still possible when the leakage inductance is poorly estimated, but the system dynamic performance will be influenced.

Measurement circuits are built to scale down the measured three-phase voltage and current to voltage signals suitable for the ADC of the DSP. The voltage measurement circuit consists of a hardware low-pass filter to get rid of the switching harmonics. To provide a faster control for the inner current control loop of the control strategy, the measured current is not filtered. When estimating the flux and position, a software filter is acted on the measured current to make sure the same phase delay in measured voltage and current. The speed and corner-frequency of the filter are known, so the FAST flux position estimation function of the C2000 DSP can compensate for this phase-delay.

When the speed of B-DFIG is similar to the nature speed (600 rpm in this thesis), the time-harmonic will be especially severe for the flux and position estimator. In that case, f_{ce} goes to zero, which is comparable to the case of controlling an induction machine around zero speed or a DFIG around its synchronous speed. The speed dependent time-harmonic in the regular induction machine will disappear when its speed is about zero, but it will be very obvious when the speed of B-DFIG is around natural speed. The induced time-harmonic voltage and current will then exceed the main voltage, confusing the position estimator and leading to the loss of synchronism. To solve this problem, a ripple filter function is applied in the software, including a phase delay free notch filter with a filter frequency being proportional to the mechanical speed. Continuous operation of B-DFIG at its natural speed should be avoided due to the difficulties of determining the flux position at this point. This will lead an unbalanced loading of the IGBT modules and increase the risk of IGBT failures.

7.5. BEHAVIOUR IN FULL VOLTAGE

IN Chapter 5.3, the performance of B-DFIG has been simulated in full voltage condition. In this section, experiment should be implemented to check the performance first and the similarity to simulation second. Figure 7.16 describes the phase current in PW and CW of B-DFIG under full voltage condition in both sub-synchronous and super-synchronous modes. The PW phase voltage is given by 100 V which is the same as that in simulation. There is not any applied load torque on the machine, so only the resistance torque of B-DFIG rotor and DC machine rotor work.

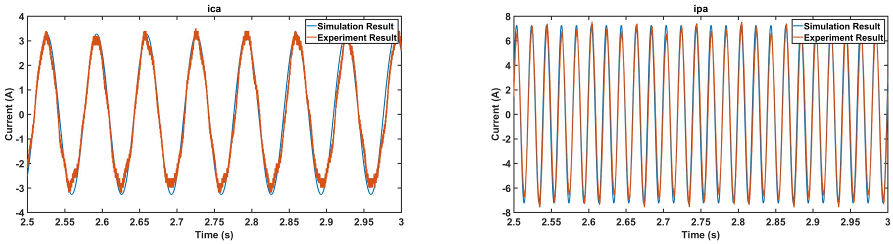

(a) CW Phase Current at Sub-synchronous Speed (420 rpm)

(b) PW Phase Current at Sub-synchronous Speed (420 rpm)

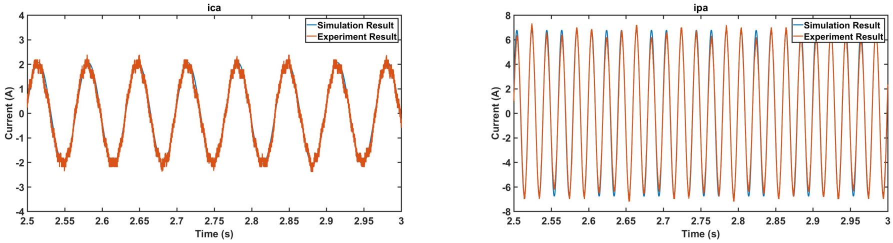

(c) CW Phase Current at Super-synchronous Speed (780 rpm)

(d) PW Phase Current at Super-synchronous Speed (780 rpm)

Figure 7.16: Phase Current of CW and PW under Full Voltage Condition in Sub-synchronous and Super-synchronous Modes

From above figures, it can be seen that the CW and PW phase current in both simulation and experiment are almost same, which means the parameters of B-DFIG and test conditions are same at simulation and experiment. In the figures of CW phase current, the period and frequency is about 0.067 s and 15 Hz respectively proved by calculations, which shows the B-DFIG runs in synchronous mode and the relationship of PW, rotor and CW corresponds to (2.13).

7.6. BEHAVIOUR IN LOW VOLTAGE RIDE THROUGH

HAVING measured the B-DFIG behaviour under full voltage condition, the performance of B-DFIG in low voltage dip should be measured. Figure 7.17 and 7.18 describe the phase current in both PW and CW under different voltage dip levels (25 % of voltage dip, 50 % of voltage dip and 75 % of voltage dip respectively) in both sub-synchronous and super-synchronous modes.

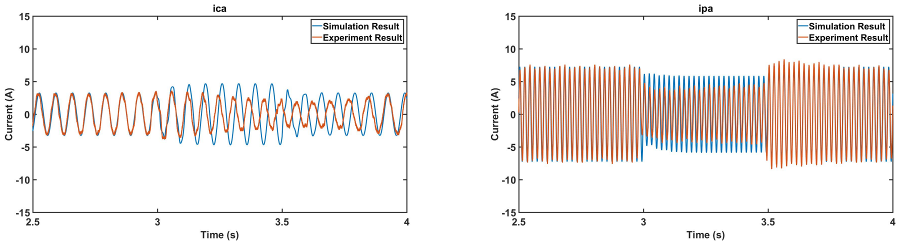

(a) CW Phase Current under 25 % of Voltage Dip (b) PW Phase Current under 25 % of Voltage Dip

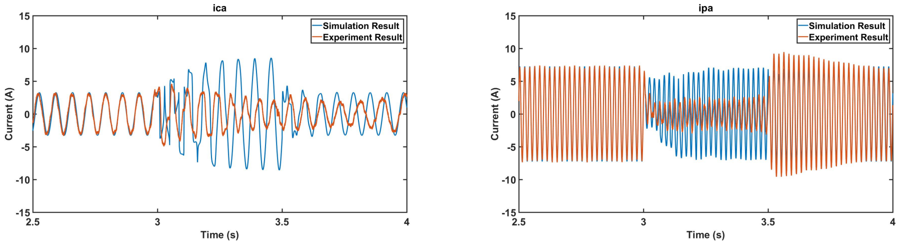

(c) CW Phase Current under 50 % of Voltage Dip (d) PW Phase Current under 50 % of Voltage Dip

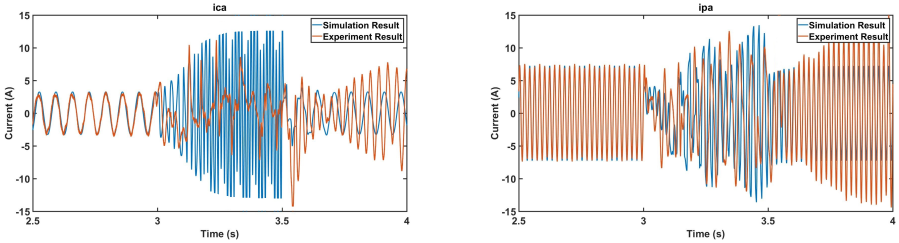

(e) CW Phase Current under 75 % of Voltage Dip (f) PW Phase Current under 75 % of Voltage Dip

Figure 7.17: CW and PW Phase Current under Low Voltage Dip Condition in Sub-synchronous Speed (420 rpm)

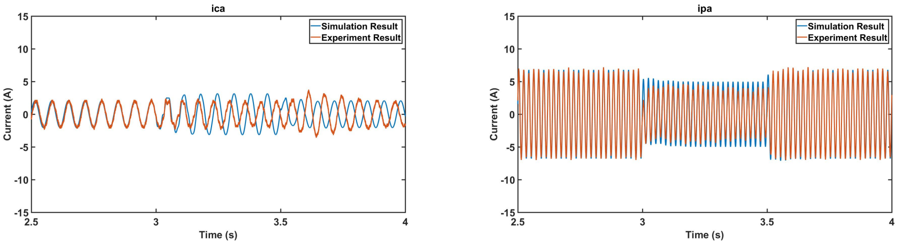

(a) CW Phase Current under 25 % of Voltage Dip (b) PW Phase Current under 25 % of Voltage Dip

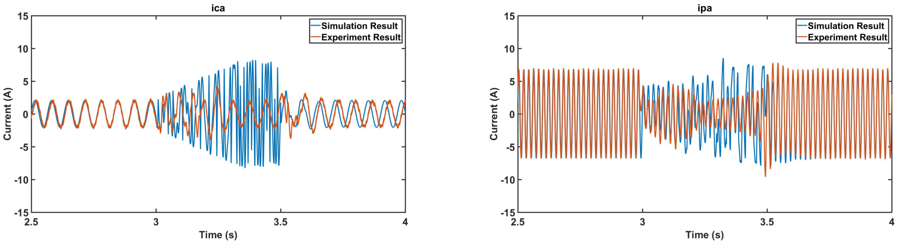

(c) CW Phase Current under 50 % of Voltage Dip (d) PW Phase Current under 50 % of Voltage Dip

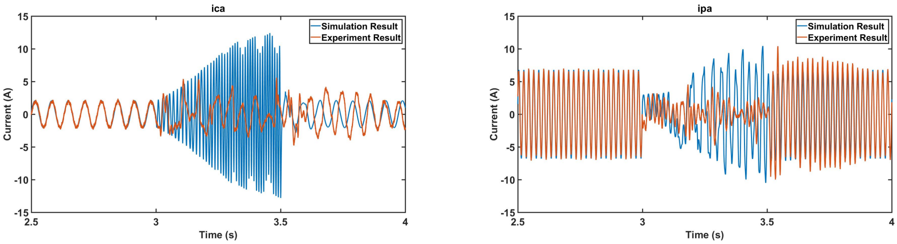

(e) CW Phase Current under 75 % of Voltage Dip (f) PW Phase Current under 75 % of Voltage Dip

Figure 7.18: CW and PW Phase Current under Low Voltage Dip Condition in Super-synchronous Speed (780 rpm)

In these figures, conclusions can be got as follows:

1. Before the low voltage dip occurs, CW phase current are the same in simulation and experiment and PW phase current too.

2. When low voltage dip occurs, PW phase current starts to decrease with the decrease of PW phase voltage. However, at this time, CW phase current will increase, because the flux decreases with the PW phase voltage dip. To produce the previous value of electric torque, CW phase current needs to increase.

3. Larger voltage dip level takes larger transient CW phase current and larger PW phase current decrease.

4. Due to time and space harmonics in experiment, the waveform in experiment result is not perfectly sinusoidal. In addition, due to speed ripple in experiment, the amplitude and frequency of PW and CW current are not constant in low voltage dip.

5. The recover time of B-DFIG in experiment is longer than that in simulation when PW phase voltage increases back to original values. In experiment, the reaction time of the controller is longer than that in simulation due to speed ripple. B-DFIG is less stable in experiment than that in simulation.

6. In simulation, all of the leakage inductance is transformed into CW while in experiment, the larger leakage inductance in rotor part will reduce the CW transient current. The equipment provides an enough dc-link voltage to the converter, so B-DFIG rides through low voltage more easily. However, in reality, dc-link voltage will decrease due to the voltage dip, so there is not enough CW phase voltage provided to the machine and CW transient current will increase very fast. In simulation, eddy current is ignored while in experiment, eddy current will produce certain power and the energy transmitted into stator winding will reduce. It also takes less stator current. In addition, the inductance of B-DFIG in PW, rotor and CW is larger than that of B-DFIG in industry, which can reduce the transient current in stator winding in low voltage ride through to some extent.

From the results in both simulation and experiment, it can be observed that the simulation condition is more ideal and the performance is better than that in experiment, because the assumptions have their limitations in reality and some factors such as time and space harmonics, speed ripple, eddy current, skin effect, slotting effect, saturation and hysteresis which are ignored in simulation cannot be ignored in experiment.

7.7. SUMMARY

MEASUREMENTS have been implemented in this chapter. Firstly, the parameters of B-DFIG in the equivalent circuit such as resistance and inductance in PW, rotor and CW are measured based on a group of tests. However, for the parameters which cannot be measured directly can be estimated in a proper way. Secondly, low voltage dip is built by the voltage divider, also including contactor control circuits. Programming microcontroller can control the power relays to switch contactors and by changing the ratios between two inductors in the voltage divider, required voltage dip levels can be got at the terminal of B-DFIG. Thirdly, Behaviours of B-DFIG under full voltage condition have been simulated and measured in the same situation to make a comparison. Finally, B-DFIG performance under low voltage dip condition is also simulated and measured in the same situation while the results are different. Analysis is given to explain the reason and it shows the ideal environment in simulation but in experiment, the result will vary a lot.

REFERENCES

[1] T. Strous, *Brushless doubly fed induction machines for wind turbine drive-train applications,* (2016).

[2] U. Shipurkar, T. D. Strous, H. Polinder, J. B. Ferreira, and A. Veltman, *Achieving sensorless control for the brushless doubly-fed induction machine,* IEEE Transactions on Energy Conversion (2017).

[3] J. Dirksen, *Lvrt low voltage ride-through,* DEWI Magazin , 56 (2013).

[4] V. Semiconductors, *Optocoupler, phototransistor output, with base connection,* 4N35 datasheet, Jan (2010).

[5] Wikipedia, *Opto-isolator — wikipedia, the free encyclopedia,* (2017), [Online; accessed 20-September-2017].

[6] P. R. PCB, *Low profile power relay with 15.7 mm height, ideal for incorporation in miniature equipment,* G2RL datasheet .

[7] Wikipedia, *Relay — wikipedia, the free encyclopedia,* (2017), [Online; accessed 20-September-2017].

[8] C. ABB, *Modular din rail components installation contactors,* ESB/EN, datasheet .

[9] Wikipedia, *Contactor — wikipedia, the free encyclopedia,* (2017), [Online; accessed 20-September-2017].

[10] Wikipedia, *Microcontroller — wikipedia, the free encyclopedia,* (2017), [Online; accessed 20-September-2017].

[11] Texas-Instrument, *Launchxl-f28027 c2000 piccolo launchpad experimenter kit,* (), user's guide .

[12] T. Instruments, *Instaspin-foc™ and instaspin-motion™ user's guide,* (2013).

8

CONCLUSION

8.1. CONCLUSIONS

This thesis focuses on the Low Voltage Ride Through (LVRT) control for the Brushless Doubly Fed Induction Generators (B-DFIG), which includes steady state modelling of B-DFIG, dynamic modelling of B-DFIG, B-DFIG control strategy, B-DFIG simulation, B-DFIG LVRT control algorithm and B-DFIG experiment.

In the steady state modelling of B-DFIG, firstly, three kinds of operating modes are described to understand this machine better. There are simple, cascade and synchronous modes and both simple and cascade modes are called asynchronous modes. B-DFIG in these modes do not have a good performance, so people are not willing to run B-DFIG in these two modes. Synchronous mode is most popular mode that people use in industry and equations between variables are given to display the principles of B-DFIG in this mode. In addition, rotating direction, speed range and torque-load angle characteristic of B-DFIG are also given to show B-DFIG is similar to a synchronous machine. Then, based on assumptions, equivalent circuits are presented which contain normal equivalent circuit, simplified equivalent circuit and Γ-equivalent circuit. These equivalent circuits are derived step by step and from complicated to simple.

In dynamic modelling of B-DFIG, firstly, differential equations are derived based on the equivalent circuit. Then according to differential equations, block diagram is built to form the dynamic model of B-DFIG. In this model, space vectors are introduced and every vector in PW, rotor and CW can be transformed into another winding by the Ideal Rotating Transformer (IRTF).

In B-DFIG control strategy, firstly, different kinds of control strategies are given which include open-loop scalar control, close-loop scalar control, phase angle control, indirect stator quantities control and vector control. The vector control can be divided into Voltage Oriented Control (VOC) and Field Oriented Control (FOC). VOC is always applied in active and reactive power control and FOC is used in speed and torque control. In this thesis, FOC is used and provides better dynamic performance, which is widely developed in conventional DFIG drive system and implementation of the sensorless DFIG control scheme. Secondly, the complete machine's model is built which contains not only B-DFIG model but also sensorless FOC, grid voltage side, power electronic converter, measurement block and mechanical system. In the sensorless FOC, there are two control loops: speed loop and current loop and two input reference signals corresponding with dq-axis: i_{cd} in d-axis controls the magnetizing current and flux and f_m in q-axis controls speed and torque. This kind of control strategy can decouple the dq-axis values completely without any cross-coupling effect. The output of the two control loops is the modulation index. Through space vector modulation, the modulation index is sent to power electronic converter. In the power electronic converter, SPWM is applied and through the comparison between required sinusoidal waveform and triangle waveform, Control Winding (CW) phase voltage can be got. Finally, control strategy performance is simulated which contains speed range simulations, current step response, speed step response and load torque step response. From these simulations, the performance of the controller can be known clearly and B-DFIG can operate at synchronous mode successfully with this control strategy.

In B-DFIG simulation, firstly, based on assumptions and constraints, behaviours of B-DFIG under full voltage condition are simulated. It can be got steady state value of Power Winding (PW) and Control Winding (CW) phase current from this simulation. Larger load torque will take larger CW current, so the largest load torque case is simulated, which is worst condition. Under this condition, if the machine can ride through low voltage, it can also can ride through low voltage successfully in lower load torque conditions. Secondly, different low voltage dip levels are simulated (25 %, 50 % and 75 % of voltage dip respectively). Finally, the performance of B-DFIG is also simulated under these low voltage dip conditions and large transient stator current is observed, which has an adverse effect on the power electronic converter.

In B-DFIG LVRT control algorithm, since B-DFIG with normal control strategy cannot ride through low voltage (the large transient CW current will destroy the power electronic converter), a new LVRT control algorithm is proposed to solve this problem. The LVRT control algorithm is injecting reactive current to the machine when low voltage dip occurs, because B-DFIG can only deliver less power to the grid in low voltage dip and the extra energy will stay at the machine producing large transient stator current. Injecting reactive current can support the grid voltage in low voltage dip and reduce the stator current in acceptable level. In full voltage condition, B-DFIG operates with normal control strategy and when the controller detects low voltage dip, it will shift into LVRT control algorithm. After the grid faults are cleared, the controller will turn back to the normal control strategy. Based on this method, behaviours of B-DFIG are simulated and CW current can be reduced in an acceptable level, which will not be harmful to the power electronic converter. Therefore, the machine does not need to be disconnected from the grid when low voltage dip occurs and it proves B-DFIG can ride through low voltage with LVRT control algorithm successfully.

In B-DFIG experiment, firstly, parameters measurement is done to provide parameters in simulation. Secondly, low voltage dip is established by the voltage divider and contactor control circuit. Thirdly, behaviours of B-DFIG under full voltage condition are simulated and measured in both simulation and experiment at same condition and the results show the consistency between simulation and experiment. Finally, the performance of B-DFIG is simulated and measured under 25 %, 50 % and 75 % of low voltage dips. Unexpected behaviours are occurring while there are differences between simulation and experiment. Due to the large leakage inductance in B-DFIG rotor, CW transient current is not very large. In addition, constant dc-link voltage in both simulation and experiment is also helpful to the machine ridding through low voltage. Reasons for the differences between simulation and experiment have been explained that eddy current will consumes certain power and less extra power transmitted into the stator winding in experiment. In addition, the inductance of B-DFIG in PW, rotor and CW is larger than that of B-DFIG in industry, which can reduce the transient current in stator winding in low voltage ride through.

In conclusion, B-DFIG has a good ability to ride through low voltage and with the LVRT control algorithm, B-DFIG operates normally at low voltage dip condition. Therefore, it can be connected to the grid when faults occur.

8.2. FUTURE WORK

Based on this thesis, a lot of possibilities can be investigated in the future work. Firstly, the LVRT control algorithm can be developed in the power electronic converter in experiment to testify the feasibility of the LVRT control algorithm in reality. Secondly, there is only machine side converter in experiment and an input dc-link is applied to produce CW voltage. However, in industry, there is a back to back converter between the grid and CW of B-DFIG. Therefore, the grid side converter should be developed and added in experiment. Thirdly, the design of B-DFIG is not optimized and the inductance of B-DFIG is higher than that in industry, so the performance of B-DFIG in experiment will be better than that in reality. Finally, only symmetrical voltage dip is studied in this thesis, because in the model of B-DFIG, the zero sequence components are considered to be zero and in asymmetrical voltage dip such as single-phase voltage dip and phase to phase voltage dip which are always occurring in reality, the performance of B-DFIG should be investigated and improved under grid faults.